

A Numerical Investigation of the Organization and Interaction of the Convective and Stratiform Regions of Tropical Squall Lines

JEAN-PHILIPPE LAFORE* AND MITCHELL W. MONCRIEFF

National Center for Atmospheric Research,[†] Boulder, Colorado

(Manuscript received 1 February 1988, in final form 5 September 1988)

ABSTRACT

A set of 13 two-dimensional numerical simulations based on the 22 and 23 June soundings from the Convection Profonde Tropicale in 1981 (COPT81) experiment in West Africa is used to study the organization and interaction of the convective and stratiform regions of squall-line-type convective systems. The initial wind profiles are characterized by the African easterly jet (AEJ) and the tropical easterly jet (TEJ) located at about 3.5 km and 14 km, respectively.

The physical processes that generate and maintain the mesoscale inflow at the rear of squall-line-type mesoscale convective systems are thereby examined. Horizontal potential temperature gradients generated by a combination of latent heat release in the convective region and unsaturated mesoscale descent, both modulated by evaporation, cause a horizontal pressure gradient and generate horizontal, line-parallel vorticity. The rear inflow is a consequence of these processes. The convective activity induces a significant upscale influence; ahead of the system the AEJ strength is reduced and the TEJ is enhanced while in the rear the TEJ is reduced. The velocity perturbation below 4 km, associated with the rear inflow, is the most marked signature in the horizontal momentum change. The effects of ice physics are examined by using a simple parameterization and the intensity of the AEJ is varied to test its effect on the rear inflow and the longevity of the convective system.

Generally, there is an extensive rotor circulation in the cold pool and the convective region consists of a series of transient convective cells traveling backwards relative to the cold pool at about 10 m s^{-1} . In many of the simulations, the inflow to the convective-scale downdraft originates ahead of the line, crosses between the transient cells and contributes to the maintenance of the cold pool and rotor. However, a significant proportion of the cold-pool mass can originate from the midlevel stratiform region, demonstrating that the longevity of the convective system is influenced by a judicious combination of convective and mesoscale processes.

The density current mechanism for maintaining the convective region of the squall line is dominant only after 3–4 h of simulation, while in the initial few hours the low-level inflow advects through the cooling region. With certain wind profiles this behavior persists throughout the lifetime of the system and a wavelike, low-level convergence (instead of a density current) organizes the development of new cells. Later stages are typified by a transition to a system having a lowered rear inflow, decreased convective depth, intensity and slope. This behavior is most pronounced for a strong AEJ.

The system-scale organization is examined by using Lagrangian conservation properties. First, passive tracer analyses quantify the relative importance of individual transports. Second, the vorticity field is analyzed by using a nonlinear steady state conservation theorem that, despite being applied to a system containing transient convective cells, adequately represents the persistent nature of the vorticity dynamics and demonstrates the strong interaction between the convective and stratiform regions.

It is demonstrated that the vorticity structure in the COPT81 lines is much more complex than a balance between the inflow shear and the vorticity generated in the vicinity of the cold pool mainly because the system-scale (convective and stratiform) baroclinic vorticity generation cannot be neglected.

Due to the form of the initial wind profiles, the simulations are directed at tropical squall lines. Nevertheless, important characteristics of midlatitude lines are also evident, such as the transient cellular convective activity and the strong rear inflow. The latter is shown to have an important effect on the convective region by enhancing the low-level convergence and the mass in the cold pool, thereby promoting a direct scale interaction. In addition, the ambient shear modulates the structure and the vorticity dynamics organizes the entire structure. General physical properties of squall lines are therefore demonstrated.

* Permanent affiliation: Centre National de Recherche Météorologique (DMN/EERM), Toulouse CEDEX, France.

[†] The National Center for Atmospheric Research is sponsored by the National Science Foundation.

Corresponding author address: Dr. Mitchell W. Moncrieff, NCAR/MMM, P.O. Box 3000, Boulder, CO 80307-3000.

1. Introduction

Squall lines in both the tropics and midlatitudes often have a stratiform region (including upper-level outflow and mesoscale descent) extending rearwards by several hundreds of kilometers. This is quite distinct from the convective region located at the leading edge of the lines, both in terms of the rainfall type and dy-

namical structure. The stratiform region is associated with ascent on a scale of several hundred kilometers. The distinction between the convective and stratiform regions in tropical squall lines has been described in Houze (1977) and Zipser (1977). Midlatitude lines show a similar behavior, as is becoming evident in several cases from the Preliminary Regional Experiment for STORM Central (PRE-STORM).

There commonly exists a marked unsaturated, warm mesoscale descent in the rear of squall lines beneath the stratiform region, for example as shown by the Zipser (1969) analysis of a squall line that occurred during the Line Islands Experiment. Conceptualization of this feature is developed in Houze (1977) and Zipser (1977). Unsaturated descent and the presence of a surface cold pool are very distinct features within the postsquall environment and these will be shown to mutually interact.

It is well established that cold and almost saturated convective-scale downdrafts are important in squall lines and that their origin and physics are quite distinct from the mesoscale descent. Numerical and analytical modeling has shown that in a propagating system, air entering the convective scale downdrafts can originate from either ahead of the line (Moncrieff and Miller 1976, hereafter MM; Redelsperger and Lafore 1988, hereafter RL) or from behind the line (Dudhia et al. 1987, hereafter DMS). However, the dynamical factors controlling the mesoscale aspects are less clear. In keeping with current terminology, the mesoscale velocity relative to the system at its rear will be referred to as the "mesoscale rear inflow" or the "rear-inflow jet." Such features have been quoted in literature for a considerable time. The midlatitude squall line conceptualization of Newton (1950) clearly depicts a rear inflow extending at least 100 km behind the line. A mesoscale rear inflow is also evident in the midlatitude squall line of Ogura and Liou (1980) and has also been shown to exist in tropical squall lines, for example in Zipser (1969, 1977). The rear inflow was, however, weak in the Venezuelan lines studied in Betts et al. (1976).

Recent work by Smull and Houze (1987a,b) and Chalon et al. (1988) gives the mesoscale rear inflow more prominence. The relative flow is clearly from rear to front and it progressively descends as it approaches the convective region. It can sometimes be weak but in other examples it has an amplitude of at least 10 m s^{-1} and extends rearwards for several hundred kilometers. Its intensity and location varies not only from one case study to another but also over the lifetime of the system. An understanding of the mechanisms responsible for the development and maintenance of the rear inflow and its interaction with the convective scale are major research objectives.

The multicellular nature of the convective region of a squall line observed in Newton (1950), Zipser (1969), and Zipser et al. (1981) amongst others is another in-

teresting aspect of squall lines. The numerical simulations of DMS quantified this convective substructure and showed that, at least in a West African environment, the convective region consists of a quasi-periodic sequence of cells traveling backwards relative to the gust front at about 8 m s^{-1} , with an average cell-development period of between 30 and 40 min. An analogous cellular structure is evident in the three-dimensional simulation of RL. Since the COPT81 dual-Doppler radar analyses show clear evidence of this multicellular behavior, there is little doubt that it is a real feature. An important class of squall lines therefore consists of a family of unsteady cells embedded within an organized mesoscale convective system.

There have been several simulations of tropical squall lines in recent years, for example MM, RL, DMS, Yoshizaki (1986), and Nicholls (1987). Redelsperger and Lafore (1988) and DMS considered squall lines over land in West Africa, observed during the COPT81, while Nicholls simulated an oceanic squall line occurring during GATE. Due to the local climatology, the environmental wind component normal to the GATE and West African squall lines have a double-jet structure, namely the African easterly jet (AEJ) and the tropical easterly jet (TEJ).

Squall lines occurring in wind profiles more characteristic of midlatitudes, particularly in strong low-level shear, were studied numerically and analytically by Thorpe et al. (1982, hereafter TMM). Recently, Rotunno et al. (1988, hereafter RKW) also addressed the role of low-level shear and hypothesized an optimal condition for long-lived convection.

A squall-line-type mesoscale convective system, composed of convective and mesoscale precipitation regions, idealistically involves two dominant scales, namely, meso- γ -scale cells and a meso- β -scale response. It will be shown that the extensive stratiform structure, the mesoscale inflow, the maintenance of the cold pool, the differential propagation of the cold pool and the convective cells and the properties that determine the travel speed of the system are *all intimately connected by the overall system-scale dynamics*. However, although the dynamical aspects are paramount it will be shown that the inclusion of ice physics makes the structure of the stratiform region more realistic.

2. Methodology

a. Model

The convective and mesoscale regions of a squall line are mutually interactive, so a large domain with an accompanying high resolution in the convective region is desirable. The Clark (1977) model was used because the interactive grid nesting (Clark and Farley 1984) facilitates a study of the scale interaction associated with an extensive multicellular convective system.

The version of the Clark model used has three interactively nested domains. Figure 1 shows the cloud mixing-ratio field for the outer domain (domain 1), the grid-nesting geometry and the scale of the system being simulated. In this figure, the system is almost stationary because a Galilean transformation has been applied to the initial wind field. Relative to the ground, however, the system moves from right to left. Three main regions are the leading anvil, the convective region and the rearward stratiform region. Domain 1 covers a large area ($480 \text{ km} \times 30 \text{ km}$) with a coarse resolution ($6 \text{ km} \times 1 \text{ km}$) to minimize the effect of the lateral boundary conditions on the inner domains. Simulations of at least 12 h duration were completed without evidence of numerical artifacts. Domain 2 defines a $240 \text{ km} \times 20 \text{ km}$ region and represents the dynamically active regions of the system and the interaction of the convective and stratiform regions with a better resolution ($3 \text{ km} \times 0.5 \text{ km}$). Domain 3 represents the convective scales with a sufficiently high resolution ($1 \text{ km} \times 0.5 \text{ km}$) over an area of $120 \text{ km} \times 17.5 \text{ km}$ and includes the entire convective region and also part of the stratiform region.

The use of interactive nesting made it possible to run an extensive series of lengthy, two-dimensional simulations and this approach is essential in the series of three-dimensional simulations also performed but not reported here. These 12 h, two-dimensional experiments in a $480 \text{ km} \times 30 \text{ km}$ domain with a resolution of $1 \text{ km} \times 0.5 \text{ km}$ in the x - and z -directions are computer-limited even on a CRAY XMP. However, the question of the effect of the multiple nesting on the nature of the solutions arises. Tests of two-domain nesting in the simpler problem of bubble collapse were

performed by Clark and Farley (1984). They showed that the mean-square temperature and kinetic energy errors in the inner domain were at most a few percent and could be much less. Such extensive tests were not performed for the present physically more complex problem in a triple-nested domain. However, the general evolution and structure of the solutions were not significantly affected as shown by Hall (personal communication). For example, the nesting only decreased the travel speed by about 1 m s^{-1} and the general morphology and evolution were only slightly altered.

In choosing the nesting configuration, the most important consideration was the position of the upper boundary of the inner domains. Tests demonstrated that the nested grid should not be configured with an upper boundary of an inner domain intersecting a convective area because spurious gravity wave reflections can occur at this boundary and affect the dynamical evolution of the entire system. The upper boundary of domain 3 was therefore located above the tropopause level of 16 km. An upper-level absorber included in the layers above 20 km in domain 1 removes the gravity waves that rigid-lid upper boundary conditions would otherwise reflect.

The open lateral boundary conditions are as in Clark (1979) except for the value of ϵ in the following equation reproduced from Cho and Clark (1981):

$$u_b^{(n+1)} - u_b^{(n-1)} = \Delta u^{(n)} = (1 - \epsilon)\Delta u^* + \epsilon(U_{\pm\infty} - u_b^{(n-1)}) \quad (1)$$

where Δu^* is given by an Orlanski type of lateral boundary condition for the velocity component normal to the line at the $(n + 1)^{\text{th}}$ time step, and $U_{\pm\infty}(z)$ is the initial wind profile to which the model relaxes. The parameter ϵ affects the rate at which the model adjusts to the specified initial lateral boundary conditions on a time scale $T = \Delta t/\epsilon$, where Δt is the integration timestep. As T increases, the predictions of the normal velocity components become more strongly determined by the internal flow and less influenced by the initial wind profile. A value of $\epsilon = 0.001$, corresponding to $T = 4 \text{ h}$ was chosen because it is well in excess of the convective time scale. However, a value of $\epsilon = 0.0001$ ($T = 40 \text{ h}$) is used in simulation 23YL to test the sensitivity of the long-term evolution to the boundary conditions. The treatment of the lateral boundary conditions is particularly relevant to squall line simulations because the velocity perturbations are of comparable magnitude to the mean flow.

b. Set of simulations

The squall lines observed on 22 and 23 June during COPT81 were selected for numerical experimentation. These have already been the subject of observational studies by Roux et al. (1984), Chong et al. (1987) for the 22 June case and Roux (1988), Chalon et al. (1988) for the 23 June case. Numerical experiments using ob-

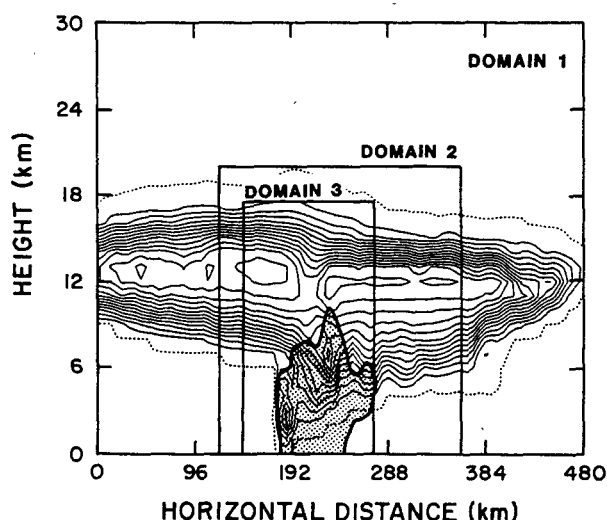


FIG. 1. Cloud mixing ratio field (q_c) for domain 1 after 12 h of simulation 23Y. The domains of the inner models (described in the text) are drawn and the heavy line represents the outline of the precipitation zone $q_c \geq 0.125 \text{ g kg}^{-1}$. The q_c isoline interval is 0.25 g kg^{-1} .

served data as initial conditions have also been performed by DMS and RL for the 22 and 23 June cases, respectively.

The main observed characteristics of these two quite different systems are summarized in Table 1. The 22 June case propagates fast, has an intense density current, strong stratiform ascent and pronounced trailing-stratiform precipitation. The initial convective instability and the midlevel dryness are not large (Fig. 2a). By contrast, the 23 June case propagates slower, contains only a moderate density current, produces more total precipitation and has a weaker stratiform ascent. The initial convective instability is substantial, demonstrated by the strong vertical θ_e gradient in lower levels (Fig. 2a), arising from the combination of very dry midlevel air and a relatively high surface value of θ_e .

The shear observed in the 0.25–3.5 km layer just ahead of the system is somewhat stronger on 22 June. The bulk Richardson number, $R = \text{CAPE} / \frac{1}{2}(\Delta U)^2$, (Moncrieff and Green 1972), where CAPE is the convective available potential energy and ΔU is the difference in the windspeed normal to the line between 0.25 and 3.5 kms is thus much less for this case ($R = 12$) than for 23 June ($R = 29$).

The convective pattern on 22 June is basically two dimensional up to a scale of a few tens of kilometers, but as shown by Chong et al. (1987), the overall structure becomes three dimensional at scales greater than 40 km. On the contrary, the 23 June case is more three dimensional at the convective scale. This distinction is indicated in Table 1 by the terminology “locally 2-D” and “locally 3-D” for the 22 and 23 June cases, respectively. As noted by Smull and Houze (1987b), both systems exhibit a rear-to-front flow which extends forward into the convective region. It apparently orig-

inates from deep within the stratiform region on 22 June, while appreciable inflow of ambient air occurs across the back edge of the stratiform region on 23 June.

A summary of the 13 numerical experiments is shown in Table 2. The 23 June case is emphasized in eight of these because its mesoscale rear inflow is stronger and more organized. Moreover, since a smaller amount of stratiform precipitation is produced than on 22 June, the details of the ice phase may be less important. The 22 June case has been used here mainly to make comparisons with DMS and to investigate the impact of the initial thermodynamic and velocity profiles.

Figure 2b shows the wind profiles used, some of which are modified forms of those observed just ahead of the system (profiles X and U for the 22 and 23 June cases, respectively). Profiles Y and Z represent an intensification of the AEJ speed (U_j) over the value occurring in profile X. The wind shear above the AEJ is, however, substantially different in profile M because the strong jet is absent.

c. Microphysical parameterizations

Certain features concerning the microphysical parameterizations were also investigated. Simulations identified with “E” use the rain evaporation parameterization of Miller and Pearce (1974, hereafter MP), in which the evaporation rate is simply proportional to the difference between the parcel and environment specific humidities. This has a substantially larger evaporation rate than the more complex scheme used in the Clark model, especially for small values of the rainwater mixing ratio.

The precipitation fall speed is reduced in the simulations identified by “I” in order to represent the dy-

TABLE 1. Comparison of the two squall line cases deduced from the 22 and 23 June COPT81 datasets (from Chalon et al. 1988). The total surface rainfall intensity ($\text{tonne m}^{-1} \text{s}^{-1}$) is estimated for a unit squall line length (1 m). The extent of stratiform and convective precipitation is estimated from the reflectivity pattern. The precipitation statistics for the 22 June case is from Chong et al. (1987) and Chong (personal communication).

Parameter	22 June COPT81	23 June COPT81
Overall structure	Locally 2D, strong stratiform part	Locally 3D, weak stratiform part
LCL (m)	350	670
LFC (m)	800	1200
$(\theta_e)_{\text{midlevel, min}} - (\theta_e)_{\text{lowlevel, max}}$ ($^{\circ}\text{K}$)	-17	-29
$\theta_{\text{density current}} - \theta_{\text{inflow}}$ ($^{\circ}\text{K}$)	-4 to -4.5	-5 to -5.5
Propagation speed and direction relative to ground (m s^{-1} , deg)	(-19, 246)	(-14.5, 225)
Total surface rain intensity (R_s) ($\text{tonne m}^{-1} \text{s}^{-1}$)	.3	.45
Stratiform precipitation	$0.4R_s$	$0.2R_s$
Convective precipitation	$0.6R_s$	$0.8R_s$
Extent of stratiform precipitation (km)	210	170
Extent of convective precipitation (km)	40	30
Maximum vertical motion in stratiform region (m s^{-1})	Ascent 0.5 Descent -0.3	0.5 -0.15
Wind shear in the 0.25–3.5 km layer (s^{-1})	4.6×10^{-3}	4.3×10^{-3}
CAPE (J kg^{-1})	1328	2810
Convective Richardson number in the 0.25–3.5 km layer	12	29

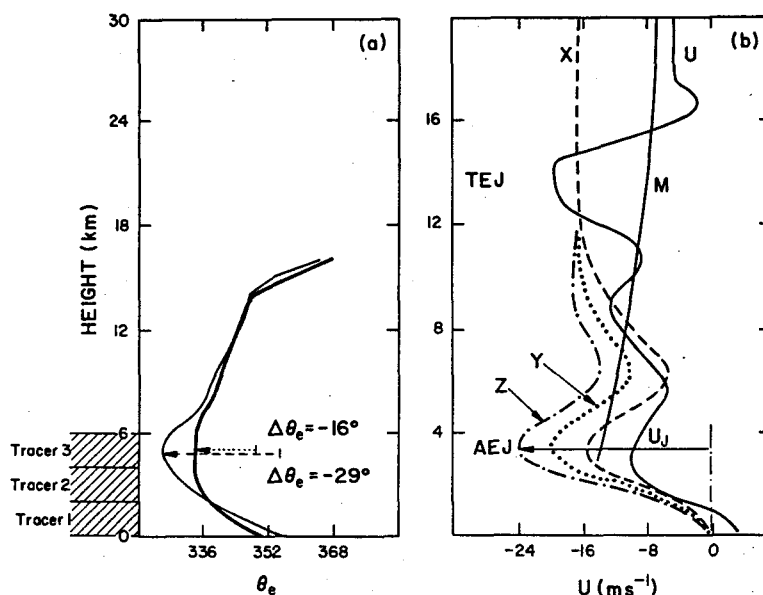


FIG. 2. (a) Initial θ_e profiles for the 22 (thick line) and 23 June cases. The θ_e profile above 17.5 km has been modified. (b) The different initial ground-relative wind profiles used in the simulations. The U and X profiles are those observed on 23 and 22 June, respectively.

namical effect of the ice phase in a simple way. The following criteria, obtained from Heymsfield (personal communication) were used to determine if the precipitation should be in the ice phase, namely if either 1) the temperature $T \leq -40^\circ\text{C}$, or 2) $-40^\circ\text{C} < T < 0$ with $|w| \leq 2 \text{ m s}^{-1}$, $\rho q_c \leq 0.5 \text{ gm}^{-3}$ and $\rho q_r \leq 1.5 \text{ gm}^{-3}$. If either condition is satisfied, then the precipitation fall speed is multiplied by the following empirical function:

$$f(z) = 0.12 + 0.88 \exp \left[\frac{-(Z - Z_{\text{bml}})}{H_{\text{ml}}} - 1 \right] \quad (2)$$

where $Z_{\text{bml}} = 3.2 \text{ km}$ is the melting layer base and $H_{\text{ml}} = 1 \text{ km}$, the melting layer depth. With this formula, a typical terminal fall speed is $0.75 \pm 0.25 \text{ m s}^{-1}$ in the ice crystal zone ($z > 7 \text{ km}$), and $1.25 \pm 0.25 \text{ m s}^{-1}$ in the aggregation zone located about 2 km above the height of the zero-degree isotherm (approximately 4.2 km). These values are confirmed by the limited amount of available observational data. The precipitation fall speed in the melting layer rapidly attains the value corresponding to the liquid phase. The accretion of cloud water is also modified by the same factor to be consistent with the above fall-speed reduction. Due

TABLE 2. Set of two-dimensional simulations performed on the thermodynamic profiles observed ahead of the June 22 and 23 squall lines. Wind profiles X and U represent conditions observed just ahead of the 22 June and 23 June cases, respectively. Wind profiles Y and Z represent a modified AEJ maximum (U_j) and profile M represents the effect of a small upper-level shear. The letters I , E , G , and L represent the empirical ice phase, the simplified evaporation scheme, a reinitialization with a mature density current and a simulation with a 40 h relaxation time constant, respectively.

Simulation	Thermodynamical profile (day)	Wind profile (see Fig. 2b)	Microphysical modification	Duration of simulation (h)
23U	23	U	—	12
23X	23	X	—	8
23Y	23	Y	—	16
23Z	23	Z	—	12
23YL	23	Y	—	16
23YI	23	Y	I	12
23UI	23	U	I	8
23M	23	M	—	8
22X	22	X	—	8
22M	22	M	—	8
22XE	22	X	E	8
22ME	22	M	E	8
22XG	22	X	—	4 (6–10)

to the empiricism, these microphysical parameterizations are inexact but nonetheless allow relevant dynamical aspects of the ice phase to be investigated. The approach is not, however, a substitute for a sophisticated ice-phase parameterization.

d. Initiation

Following the approach used in DMS, an initial cooling is superposed on an initially horizontally homogeneous atmosphere defined by either the 22 June or the 23 June thermodynamic profiles observed in front of the system (Fig. 2a) and by one of the wind profiles defined in Fig. 2b. The source has a constant cooling rate of $-0.01^{\circ} \text{ s}^{-1}$ maintained for 10 min over a region of length 12 km and depths of 3 or 4 km for the 22 and 23 June cases, respectively.

e. Evolution of the control simulation

Before making comparisons, the evolution of the control simulation (23Y) is considered. This simulation best approximates the observations not only in terms of the total rain intensity and propagation speed (see Table 1), but also the mesoscale ascent detailed in section 3. The observed wind profile (U) would be the most obvious one to use in a control simulation. However, since it was taken only about 10 km ahead

of the gust front, and considering the significant upstream influence of the system, this is thought to be an unrepresentative initial profile. As shown by Chalon et al. (1988), the 23 June squall line was accompanied by a meso β -scale perturbation of the horizontal wind, characterized by a decrease in the AEJ speed and an intensification of the TEJ ahead of the system while the converse situation prevails behind the system. *The simplified profile Y therefore better represents the initial large-scale wind structure than the profile U.* For this reason, 23Y will be identified as the control for the 23 June case. Figure 3 shows examples of the evolution of the total rain intensity, the vertical velocity extrema within domain 3 (convective scale), domain 3 mean vertical motion and the propagation speed of the gust front. A marked long-period variability exists with a transition of the system structure after 12 h of simulation. The mesoscale ascent begins to decrease after 10 h, preceding the weakening of the convective activity by about 2 h.

3. Flow modification by the convective system

The vertical transport of horizontal momentum and the generation of horizontal momentum by the pressure gradient in squall lines can result in velocity perturbations comparable to the mean undisturbed flow. Observational evidence of countergradient transport

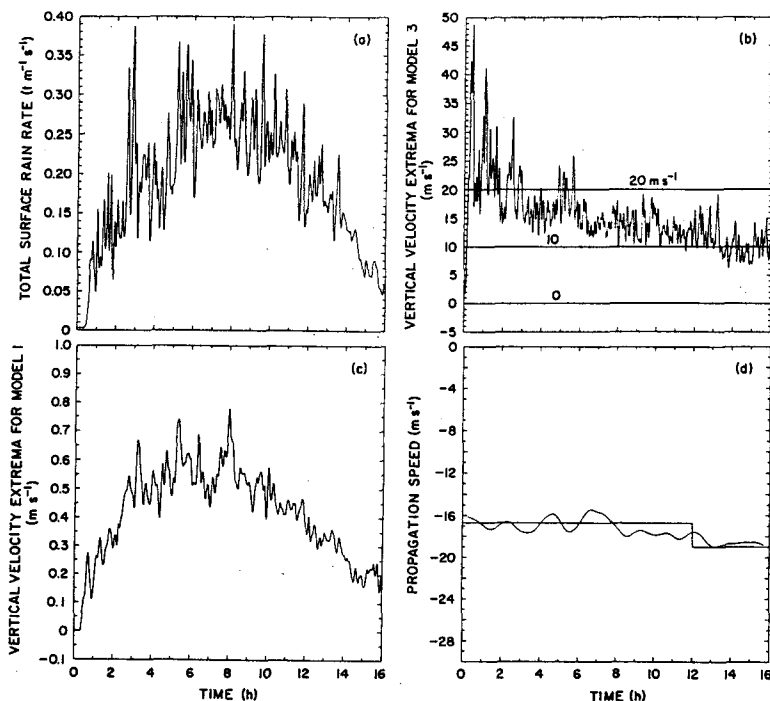


FIG. 3. Evolution of selected fields for simulation 23Y: (a) the total surface rain intensity ($\text{tonne m}^{-1} \text{ s}^{-1}$); (b) the vertical velocity extrema (m s^{-1}) for domain 3; (c) the vertical velocity extrema (m s^{-1}) averaged over domain 3 (120 km); (d) the gust front propagation speed (m s^{-1}) and the model Galilean transformation, shown by the horizontal lines.

of momentum in squall lines was given in LeMone (1983) and Soong and Tao (1984). A theoretical rationalization of the dynamical aspects of organized momentum transport and the relative importance of the generation of momentum by the horizontal pressure gradient and momentum transport by velocity correlations was demonstrated in Moncrieff (1981).

The combined effects of momentum transport and pressure-induced momentum changes per unit mass are most conveniently measured as the difference between the simulated and initial horizontal velocity components.

a. Modification of the horizontal wind component during the mature stage

As stated above, major upstream and downstream flow modifications are evident. In Fig. 4a, the horizontal component of velocity averaged between 8 and 10 h in simulation 23Y shows features typical of the mature stage. The extensive rear-to-front relative flow in the 2–4 km layer has a shallow slope except in the neighborhood of the leading edge. The front-to-rear

flow that represents the upward and rearward displacement of boundary-layer air is also pronounced. Both of these features are found in observations (Smull and Houze 1987b and Chalon et al. 1988).

The wind perturbation from the initial wind field in domain 1 is shown in Fig. 4b; there is a marked asymmetry due to the vertical shear. (Herein, the terms “perturbation” and “buoyancy” refer to differences from the initial conditions rather than differences from time-dependent horizontal averages). All the simulations exhibit the following basic pattern. First, in the convective region between about 190 and 230 km, there is a strong rear-to-front, low-level perturbation associated with the rotor and an intense front-to-rear perturbation supporting the convective-scale mean ascent via low-level convergence at the leading edge. Transient effects are locally significant in the convective region, and are essential to the downdraft “cross-over zone” defined in RL and also evident here. Second, the AEJ speed is reduced ahead of the system. Third, the intense horizontal divergence above 6 km results in a TEJ intensification ahead of and reduction behind the line. Fourth, the rear-to-front perturbation below 4 km, extending up to the rear lateral boundary some 300 km behind the gust front, is the most prominent feature in the rear of the squall line system.

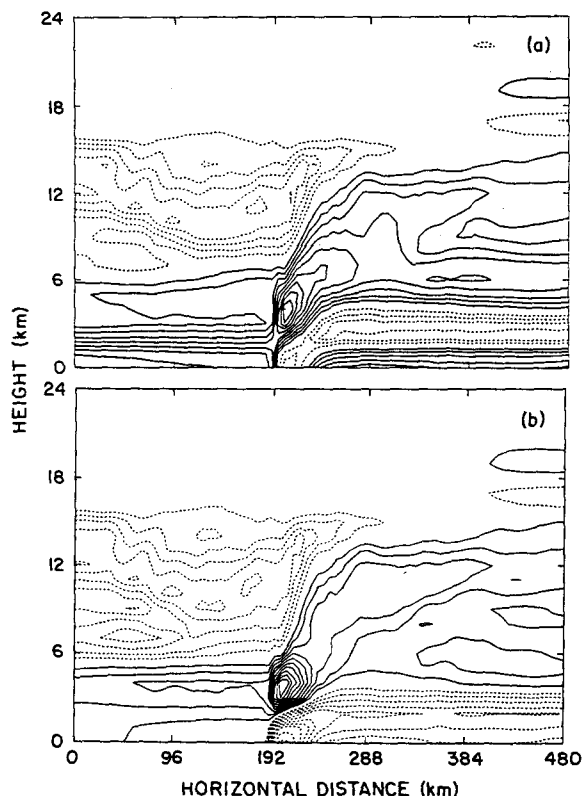


FIG. 4. (a) Horizontal component of the wind velocity relative to translation speed the model frame (-16.7 m s^{-1}); (b) the perturbation of the horizontal component of the wind velocity from the initial wind profile. The fields are for simulation 23Y (domain 1) averaged between 8 and 10 h. The contour interval is 2 m s^{-1} with the first solid line at 1 m s^{-1} and the first broken line at -1 m s^{-1} . In this and later figures the broken lines represent negative values.

b. Evolution of the horizontal wind component averaged over 2 h periods

The 2 h time-averaged fields for simulation 23Y in Fig. 5 show the evolution of the horizontal wind in domain 2 and further demonstrate the basic pattern and its intensification. In the convective region, the low-level, rear-to-front and the midlevel, front-to-rear perturbation couplet amplifies and broadens with time. The well-defined rear-to-front perturbation below 4 km intensifies and has an extreme at a height of about 2 km, coincident with the initial wind-shear maximum. The wind modifications clearly originate in the neighborhood of the convective region and subsequently extend into the far field. This demonstrates that *the rear inflow is a direct effect of convection and therefore need not involve baroclinic processes associated with synoptic gradients of potential temperature*.

c. Evolution of the wind perturbations at the rear boundary

The evolution of the horizontal wind perturbation at the rear lateral boundary of domain 1 is measured by ΔU_{\min} , the enhancement of the easterly jet compared to the initial value. The absolute value of this enhancement in Fig. 6a shows a monotonic increase over a period of 8 h. Simulation 23YL, that differs from simulation 23Y only through the value of the relaxation time scale ($T = 40 \text{ h}$), has stronger wind perturbations resulting in a more intense, better or-

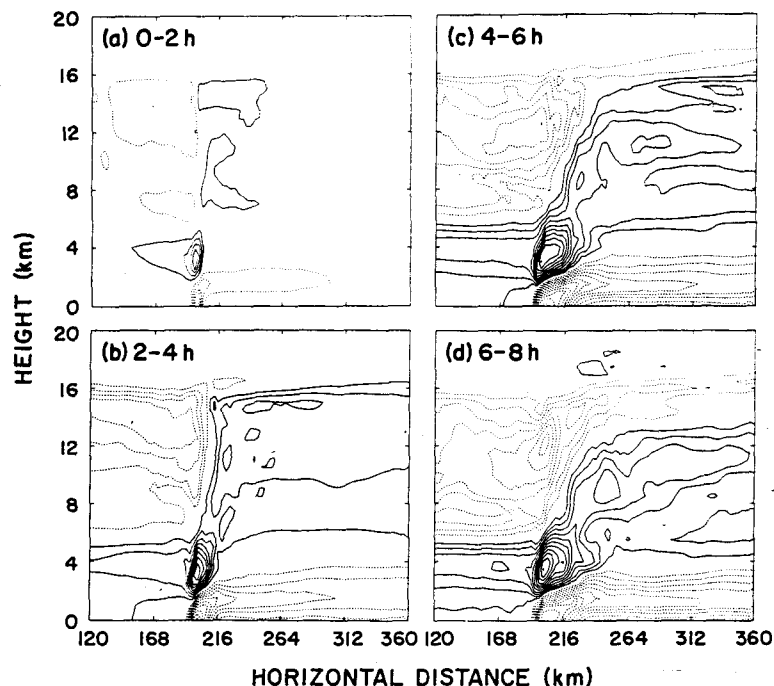


FIG. 5. Horizontal component of the velocity perturbation from the initial profile in the domain 2 for simulation 23Y averaged during (a) 0–2 h, (b) 2–4 h, (c) 4–6 h and (d) 6–8 h. The contour interval is 2 m s^{-1} with the first solid line at 1 m s^{-1} .

ganized and longer lasting system. The wind perturbation is a linear function of the initial AEJ intensity (U_j) as shown by Fig. 6b. Comparison of 22X and 23X shows that a decrease in CAPE weakens the rearward wind perturbation. If the rain evaporation is enhanced (22X vs 22XE), this perturbation also increases slightly. In general, a mesoscale downdraft exists below 4 km and the perturbation maximum coincides with shear and subsidence maxima. There is a combined increase of the AEJ strength behind the system and a subsidence which locally lowers the jet. This has the effect of increasing the low-level convergence and suggests that a *horizontal convergence enhancement caused by the intensification and subsidence of the AEJ* may play a role in the maintenance of the squall line, particularly the generation of new cellular activity.

Figure 7a shows an absolute intensification of the AEJ up to the maximum value at the rear of domain 1 for the 23 June simulation. This acceleration depends weakly on the initial AEJ speed and has a magnitude of about $1 \text{ m s}^{-1} \text{ h}^{-1}$. A reduction of the difference between the speeds at 500 m and at the AEJ maximum about 50 km ahead of the gust front, evaluated at the front of domain 3, is shown as a function of the initial AEJ speed in Fig. 7b. These changes in the AEJ speed (and those in Figs. 4b and 5) are consistent with observations because Chalon et al. (1988) noted a 5 m s^{-1} AEJ reduction ahead and an enhancement behind the system, i.e., a reinforcement of the easterly winds on the approach of the squall and a subsequent post-

system weakening. Chalon et al. (1988) estimate that these variations are on a scale of 600–800 km, which is comparable with the present simulations. The two-dimensional assumption, however, probably accentuates the amplitudes of the perturbations. Smull and Houze (1987b) also noted an acceleration of the relative flow toward the system ahead of the squall line (see their Figs. 7 and 8). In ground relative terms this involved a reduction (and ultimately a reversal) of the prevailing midlevel westerlies.

d. Generation and maintenance of the mesoscale rear inflow

The pressure field and its evolution is not easy to interpret because it is intimately related to the momentum flux. A dynamically satisfactory explanation requires consideration of the system-scale structure, for instance following the nonlinear conservative approaches of sections 5 and 6. The pressure perturbation field (Fig. 8a) can, however, diagnostically explain the rear-to-front wind modification and the AEJ intensification. The low pressure centered at 2 km associated with the convective region and overlying the surface high, is in good agreement with observations (LeMone et al. 1984 and RL). At larger scales behind the convective zone, a front-to-rear, midlevel pressure gradient of about 0.5 mb magnitude (representing a rear-to-front acceleration) over 300 km exists. Recent progress in retrieval techniques in the stratiform region may

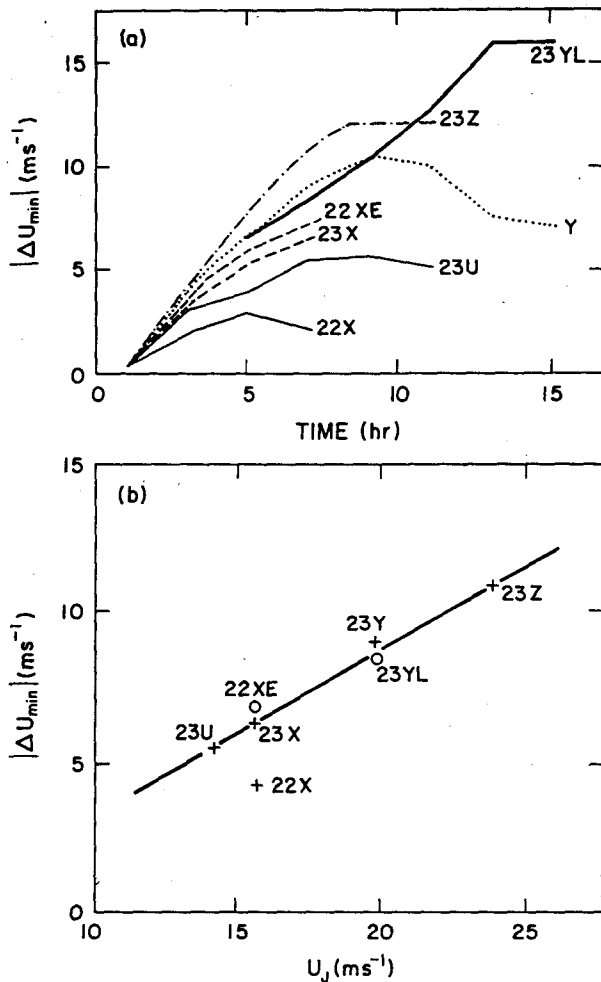


FIG. 6. (a) Evolution of the $|\Delta U_{\min}|$ at the domain-1 rear lateral boundary for different simulations. (b) Dependency of the perturbation on the initial AEJ maximum speed (U_j) after 7 h of simulation.

allow such a gradient to be detected via Doppler radar observations (Matejka, personal communication).

Outside the convective region the pressure can be shown to be approximately hydrostatic and, consequently, the pressure field (Figs. 8a and c) can be legitimately calculated by a downward integration of the full buoyancy field (Figs. 8b and d) from the model top. (The full buoyancy field includes the temperature and vapor mixing ratio perturbations and the cloud-water and precipitation drag.)

In Fig. 8b and d the density current has the characteristically deep head and shallower tail regions while the warm zone above 4 km is due to latent heat release. The subsidence between 1–4 km to the rear of the convection causes an extensive adiabatic warming with a maximum at about 60 km behind the gust front in 23U. At this locality the warming is about 0.3 K h^{-1} in the absence of significant evaporative cooling. The ice representation (23UI) enhances the subsidence (-3

to -12 cm s^{-1}) and the adiabatic warming (1.2 K h^{-1}). The increased evaporation rate (-0.7 K h^{-1}) is insufficient to compensate for the enhanced adiabatic warming. The simulations 23Y and 23YI give similar results except that all intensities are doubled.

The rear-to-front, mesoscale pressure gradient below the stratiform region is a direct consequence of the rearward buoyancy decrease above 4 km. This mechanism is schematically shown in Fig. 9. The stratiform region, thicker in terms of positive buoyancy and the greater subsidence between 1.5 and 4 km in the region just behind the convective region combine to create the lowest pressure in the stratiform region; this is supported by the observations of Smull and Houze (1987a) as can be seen in their Fig. 12. The density current locally increases the pressure and decreases the horizontal pressure gradient below 1.5 km. It follows that processes that alter the local temperature and water substance such as radiative flux divergence and ice physics should influence the intensity of the rear-inflow jet.

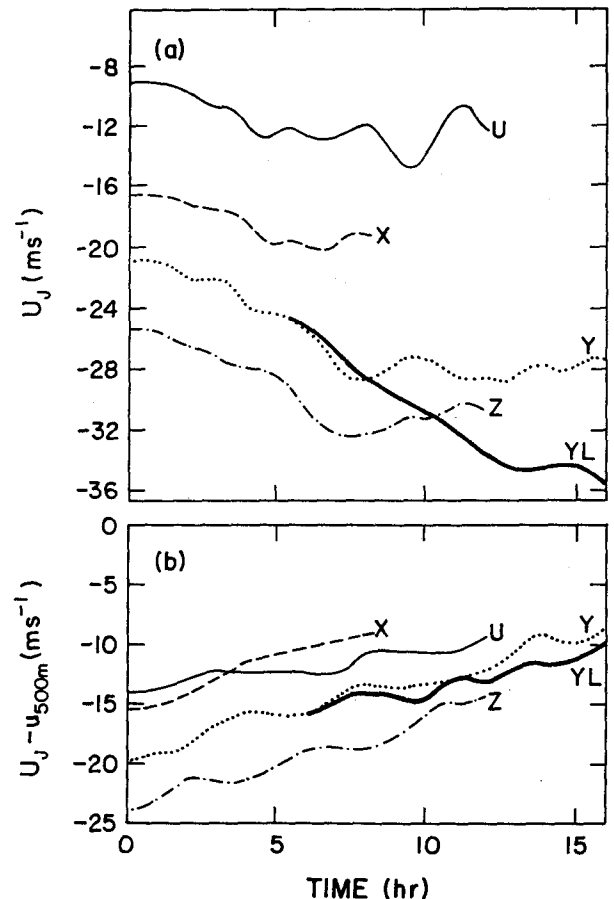


FIG. 7. (a) Evolution of the ground-relative AEJ speed at the domain-1 rear boundary for different simulations with the 23 June thermodynamics. (b) The evolution of the difference in the wind speed at the AEJ and the 500 m heights at the domain-3 front boundary. A filter with a 62 min cutoff has been applied.

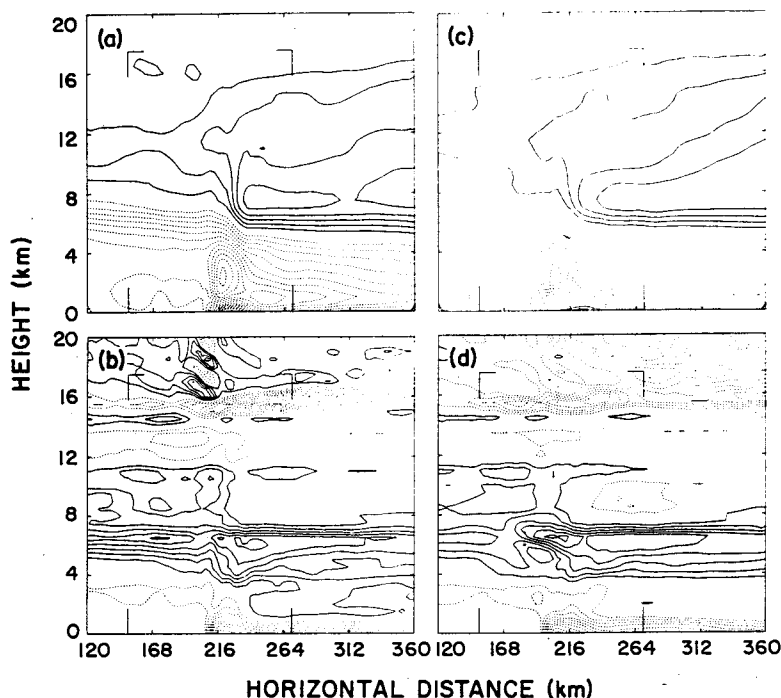


FIG. 8. (a) Pressure perturbation field for 23U, (b) full buoyancy field for 23U, (c) pressure perturbation field for 23UI, and (d) full buoyancy field for 23UI. Fields are averaged between 4 and 6 h, the pressure and buoyancy isoline intervals are 0.125 mb and 0.5°C , respectively (the first solid line is at 0.25°C). The fields are for domain 2 with the inner bracketed region corresponding to domain 3. Positive (negative) values are represented by full (broken) lines.

Simulation 23UI verifies the role of ice physics and its effect on the buoyancy and pressure fields (Figs. 8c and d). The ice distribution is depleted rearwards, consistent with Smull and Houze (1985) and the ki-

nematic model of Rutledge (1986). The location of the rain evaporation and its intensity is evident in the full buoyancy field (Fig. 8d). The mesoscale subsidence is stronger but not as warm because of enhanced evap-

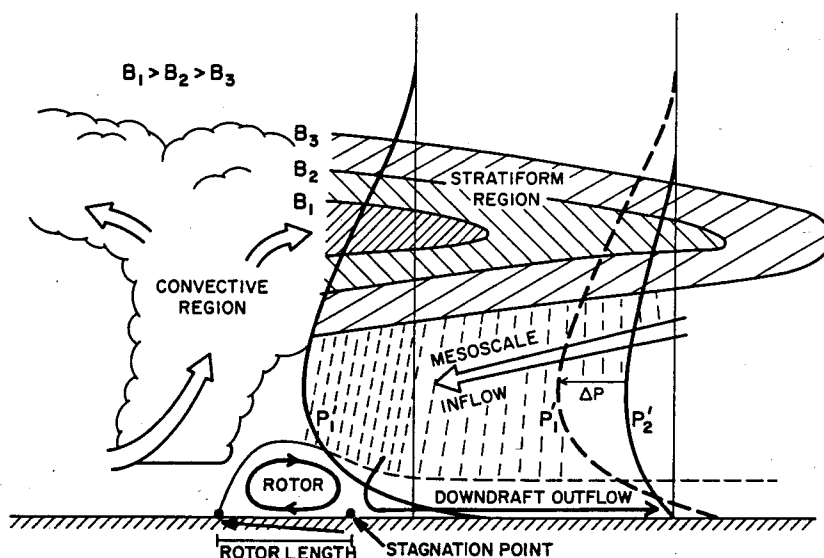


FIG. 9. Schema of the relation between buoyancy and the pressure perturbation fields in the mesoscale region of the squall line. Here B_1 , B_2 and B_3 represent the full perturbation buoyancy fields as defined in the text.

oration. The midlevel pressure gradient is consequently much weaker and not as well organized, while below 3.5 km the depleted mesoscale subsidence warming prevents an enhancement of the pressure gradient. It is interesting that this is a significantly different result from that obtained by Chen and Cotton (1986) who showed that the inclusion of ice-phase physics led to an increase in the strength of the stratiform region velocity perturbations (including the rear inflow). This was attributed to the generation of horizontal pressure gradients by a line-normal gradient in cooling due to melting of stratiform precipitation. This contradiction can only be resolved by a more complete treatment of ice-phase microphysics and it is possible that the results may be modified, perhaps in ways different from those suggested by the 23YI and 23UI simulations.

e. Mesoscale vertical motion

Large-amplitude gravity waves exist within the stratiform region. Although it is realized these are intimately involved with the far-field evolution, a detailed discussion is beyond the scope of this paper. The analysis of the mean vertical motion in the stratiform region is not easy because of its small magnitude and modulation by the gravity waves. For this reason, 4 h time- and 30 km space-averaged vertical motion fields were produced. Figures 10a and b represent profiles of these fields at 30, 60, 90 and 120 km behind the gust front for simulations 23Y and 23YI, respectively. At 30 km behind the convective region in simulation 23Y, the profile is comparable to that derived from observations by Gamache and Houze (1982), Chong et al. (1986) and Chalon et al. (1988). Subsidence (-0.3 m s^{-1}) exists below 3–4 km with ascent (0.5 m s^{-1}) above, a feature that rapidly decays rearwards. On the contrary, simulation 23YI contains a better organized and broader ($\approx 100 \text{ km}$) mesoscale subsidence, in better agreement with observations. Nevertheless, the mesoscale ascent is still too weak and localized by comparison to observations.

The descent of the rear inflow jet, representing mesoscale subsidence, is clearly evident in Figs. 11a and b for 23Y and 23YI, respectively. For simulation 23Y, the rear-to-front circulation begins to descend at about 60 km behind the gust front in a region of locally enhanced subsidence. On the contrary, in simulation 23YI the rear inflow begins to descend at 150 km behind the gust front and its thickness is reduced by differential vertical advection. The convection is also deeper in the 23Y simulation, corresponding to the longer duration of this case compared to 23YI.

4. Convective-scale dynamical structure

The organization of the convective-scale features of a squall line system is fundamentally influenced by the dual role of the cold pool and the convective cells. [The phrase "cold pool" will be used as a generic term to

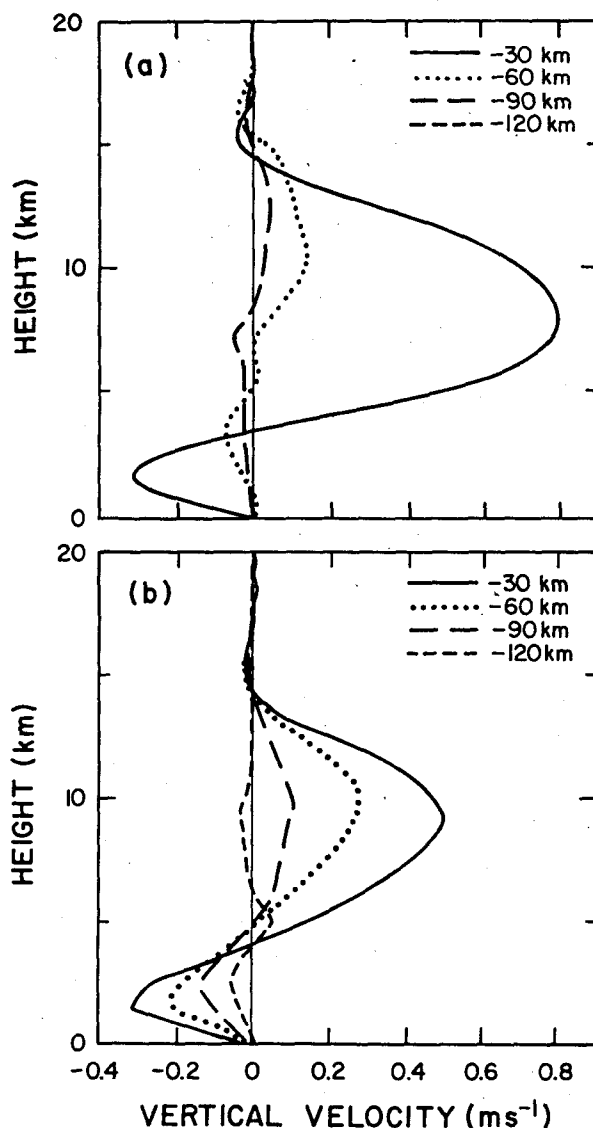


FIG. 10. (a) Time- (4–8 h) and spatially (30 km) averaged vertical velocity profiles in the rear of the squall line for simulation 23Y for different vertical sections (30, 60, 90 and 120 km) behind the gust front. (b) As in (a) but for simulation 23YI.

include 1) a density current characterized by a surface, rear-to-front relative inflow in the direction of propagation, and 2) a periodic or solitary gravity wave distinguished by having a front-to-rear relative flow passing through the cold air. The presence of a surface stagnation point and flow separation is crucial in the former.] In DMS and in the present set of simulations, both types of cold pool were identified but the density current was the most prevalent and a rotor usually existed behind the gust front.

a. Cold pool structure and dynamics

As demonstrated by numerous previous observations and simulations, the majority of mature squall lines

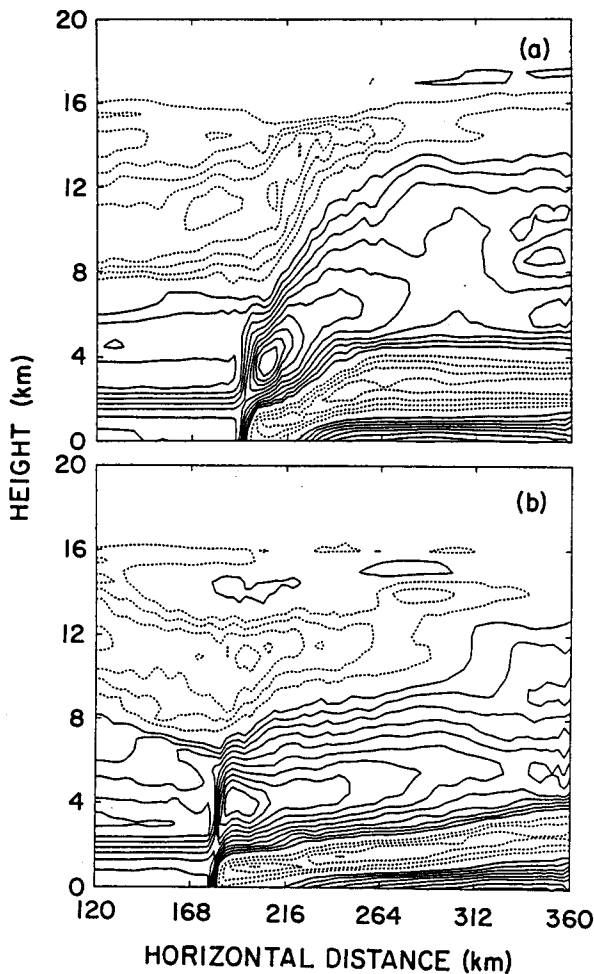


FIG. 11. Horizontal component of the wind field relative to the translation speed of the model frame of reference (c) time-averaged between 8 and 10 h in domain 2 for simulations (a) 23Y, $c = -16.7 \text{ m s}^{-1}$ and (b) 23YI, $c = -18.2 \text{ m s}^{-1}$. The isoline interval is 2 m s^{-1} with the first continuous line at 1 m s^{-1} .

contain a density current. This is also true of most (but not all) of the simulations considered here. For example, in Fig. 8b the density current head is deep and includes a rotor, while the tail is shallower with a rearward outflow circulation similar to the lines previously simulated in DMS and RL. In order to quantify the density current intensity, the mean potential energy within its head part of depth h is computed, including the effects of cloud- and rain-water drag. The variable,

$$C_* = - \left[-2g \left(\frac{\theta'}{\theta_0} - q_r - q_c \right) h \right]^{1/2}$$

proportional to the von Kármán (1940) density current propagation speed was calculated and will be called the equivalent density current propagation speed. Note that the relationship between C_* and the system propagation can be quite complicated as demonstrated by Moncrieff and So (1989).

Figure 12a represents the evolution of C_* for simulations using the 23 June thermodynamic profile. The initial value corresponds to the cooling introduced to initialize the system. During the first 90 min, the initial cold pool collapses and diverges, so $-C_*$ rapidly decreases. Subsequent to the development of precipitation, the density current intensifies through the effect of evaporative cooling and so $-C_*$ increases. The rate at which the cold pool evolves into a density current (associated with the development of a stagnation point and flow separation) increases with the intensity of the initial AEJ speed (profiles U, X, Y, and Z). Three other influences also enhance the density current formation rate, represented by the downward curve slope in Fig. 12a: a reduction in the precipitation fall speed (23YI), the shear above the AEJ (profiles M, U and X), and an increase in the rear-to-front midlevel circulation at large scale (23YL).

The evolution of C_* for the simulations based on the 22 June thermodynamic profile is shown in Fig. 13a. The density current is generally weak, consistent with the midtroposphere being too moist to allow substantial rain evaporation. If evaporation is increased by using the MP parameterization (22XE), the density current resembles that of DMS in which this parameterization is used. Furthermore, if the wind profile M is used in addition to the rain evaporation modification (22ME), again as in DMS a wave-type cell generation replaces the density current.

Figures 12b and 13b show the evolution of the cold-pool propagation speed, estimated from the gust front position at the first level in the model. Note that this is not necessarily identical to the speed of the leading edge of the most intense precipitation which is more closely related to the travel speed of the convective cells, at least on a time scale of a few tens of minutes. As was explained in DMS, the differential propagation ($\sim 10 \text{ m s}^{-1}$) of cells and cold pool (or gust front) enhances the rotor circulation. Since the travel speed of the cold pool is basically modulated by the surface wind speed (in more generality by a Froude number), while the midlevel winds control the movement of the convective cells, it follows that *the wind shear in the entire troposphere should be considered in the interaction of the cold pool and the convective cells*. This is in contrast to the theory espoused by RKW who maintain that the low-level shear is sufficient to ensure the longevity of squall lines; this aspect will be later considered in more detail.

Different types of behavior can be identified by referring to Figs. 12a and d, 13a and d. First, if C_* is equal to or greater than the system propagation speed, the system behavior is largely controlled by a density current as in the majority of the 23 June simulations after the first few hours. Second, a density current may exist but be too weak to fully influence the system propagation, as is generally true during the first few hours of the simulation when a wave-type propagation

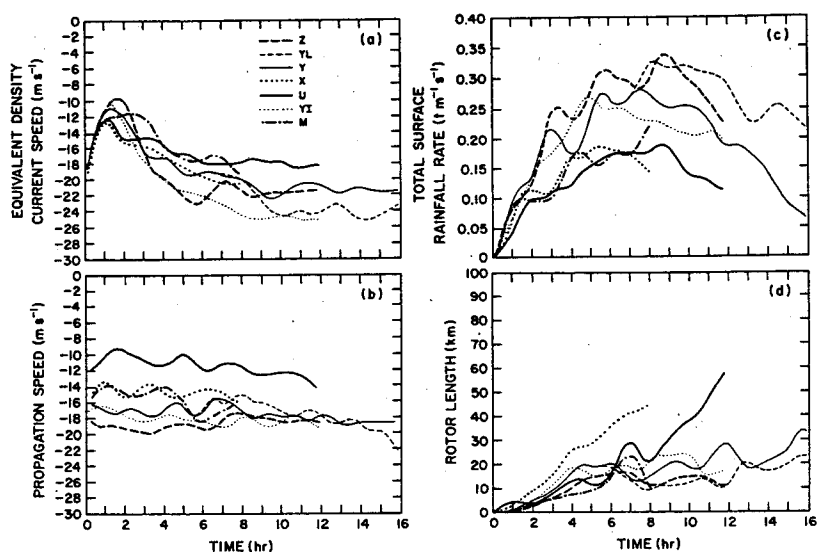


FIG. 12. The evolution of seven of the simulations with the 23 June thermodynamics: (a) The equivalent mean density current propagation speed (C_*) in m s^{-1} , (b) the propagation speed of the system (m s^{-1}) as measured by the speed of the cold pool, (c) the total rain rate ($\text{tonne m}^{-1} \text{s}^{-1}$), (d) the rotor length (km). A filter with a 62 min cutoff has been applied to the fields.

dominates. Third, the density current does not exist throughout the whole simulation but the system propagation is stable and fast, as in simulations with the 22

June thermodynamics and certain wind profiles (the M-profile in particular). In the latter, the density current is replaced by a wave type of regeneration and the

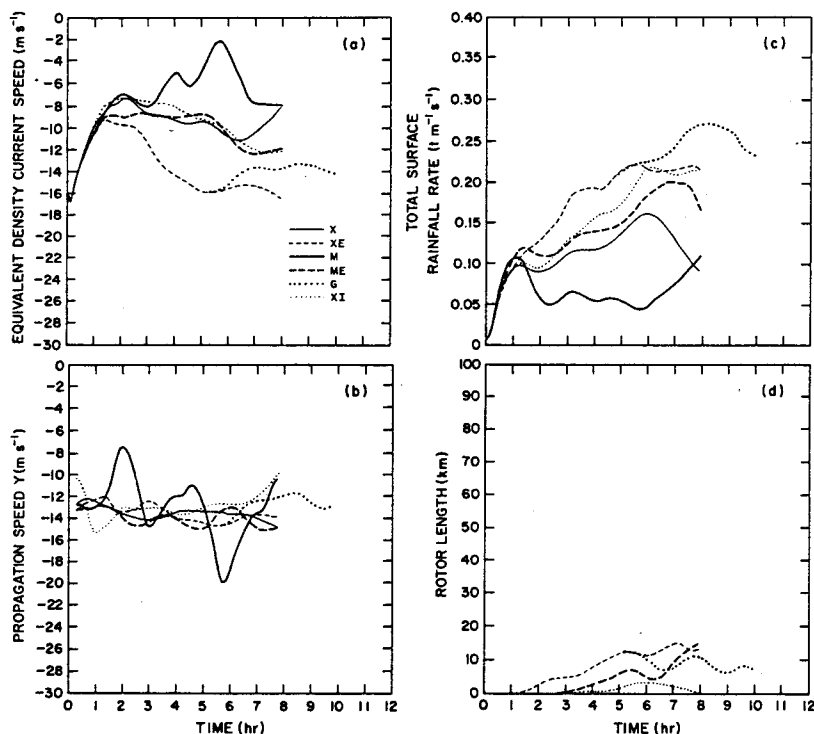


FIG. 13. As in Fig. 12 but for the simulations with the 22 June thermodynamics.

convective region consists of basically unicellular updrafts and downdrafts. Moreover, a rotor is absent and there is a strong rearward-moving surface outflow.

The rotor in the density current in Fig. 9 is driven by the water loading and evaporation associated with the mature convective cells. The length of the rotor is defined as the distance between the two stagnation points in this figure. The rotor allows air to remain beneath the heavy precipitation zone and thus be strongly cooled even with a small rain evaporation rate and the consequent strong horizontal potential temperature gradients cause a marked generation of vorticity. Figures 12d and 13d confirm the effect of the reverse shear of the inflow air above the AEJ maximum on the dimensions of the rotor. Enhancement of this shear increases the rotor length (23M, 23U and 23X). However, an increase in the amplitude of the AEJ leads to a decrease of the rotor length (23X, 23Y and 23Z). In the latter set of simulations, however, a shortening of the rotor coincides with a decrease in the upper wind relative to the AEJ. These results show that the amplitude of the AEJ and the shear above it have contrasting effects on the rotor dynamics, evidence of the highly nonlinear nature of the problem.

The wave type regeneration is favored by a moist midtroposphere but the form of the wind profile (vertical shear) is crucial. In particular, the shear above the AEJ should be weak [$\sim 1 \text{ m s}^{-1} (100 \text{ mb})^{-1}$] because well-defined jet profiles tend to produce robust density current development. It is significant that even with an enhanced rain evaporation, it was impossible to produce a density current in 22ME. Moreover, 23M is consistent with this result since only a weak density current can be produced even with substantial midlevel dryness. Precipitation loading helps maintain an intense downdraft in the updraft proximity, a characteristic feature of this type of behavior.

The surface rainfall rate shown in Figs. 12c and 13c is a direct measure of the overall convective intensity and shows that the cases with the 23 June thermodynamics are the most active, as to be expected from the enhanced values of CAPE. Note that any one of the simulations produces at best only 70% of the observed surface rainfall.

Interestingly, when simulation 22XG is initialized with the 6 h fields from 22XE, a density current similar to that observed is produced. Thus, 22XG can maintain but cannot establish a density current, demonstrating that squall lines may *persist and propagate under conditions far less favorable than those necessary for their development*.

The two basically different types of cold pool behavior are illustrated in Figs. 14a and b, 14c and d. These respectively refer to cases where a density current (23U) and wave-type surface convergence (22ME) are the primary forcing mechanisms for the convective cells. In Fig. 14a, the low-level convergence is continuous in time and about twice as strong as in Fig. 14c. The band becomes discontinuous in time above an

altitude of 2 km and an unsteadiness arises in the form of an approximate 30 min periodicity in the development of new convective cells and convective-scale downdrafts. These cells travel backwards relative to the gust front at a speed of about 10 m s^{-1} in Fig. 14b.

A transition of the system slope results when the distance between the gust front and the mature cells exceeds about 30 km (associated with a long rotor). The shear above the AEJ is important to the cell speed, the vertical tilt of the system and the rotor intensity. The rotor is enhanced if the precipitation maximum is located well behind the gust front. The remarkably persistent phase-lagged development of updrafts and downdrafts demonstrates that the quasi-periodicity is correlated with the unsteadiness of the convective downdraft inflow. This hypothesis is quantified in the tracer analyses reported in the next section.

Referring to the wavelike regeneration evident in Figs. 14c and d, a typical cell has a lifetime of about 20 min and is vertically oriented, deep and intense. It travels rearwards at only about 4 m s^{-1} relative to the surface convergence (there is no marked gust front). The surface convergence is discontinuous in time and there is a distinct wave-type propagation with new cells being initiated with extraordinary regularity at 12 min intervals. This is a variant of the wave type behavior reported in DMS where a quasi-steady solitary type of wave instead of a periodic redevelopment was identified. The solitary wave behavior is a special case due to the stationarity of the cells relative to the surface convergence field.

Generally, such wavelike behavior of the cold pool dominates during the first 2–3 h of the simulations. However, as noted by DMS, the observational evidence of this phenomenon is limited, although Fankhauser (personal communication) has detailed confirmation of this behavior in a squall line analyzed from the 20 June 1981 Cooperative Convective Precipitation Experiment (CCOPE) data. At least two logical reasons exist for the paucity of observational evidence. First, this behavior could simply be a model phenomenon, for instance a product of the cold sink initiation. However, if this is the case then the flow must retain a memory of the initial conditions for a period unreasonably far in excess of the advective time scale of the airflow through the cold pool. Second, observational analyses of squall lines have concentrated on their mature phase with a relative neglect of the development phase. It is considered that the second reason is the more plausible. Thus, detailed measurements of the flow fields near ground level are essential because this is where the distinction between the two types of behavior is the most apparent. In either case, the role of cold pool dynamics in convective initiation and maintenance is still not adequately understood.

b. Convective transition

The transition of a simulated squall line to a more horizontally orientated (i.e., weakly sloped) entity is

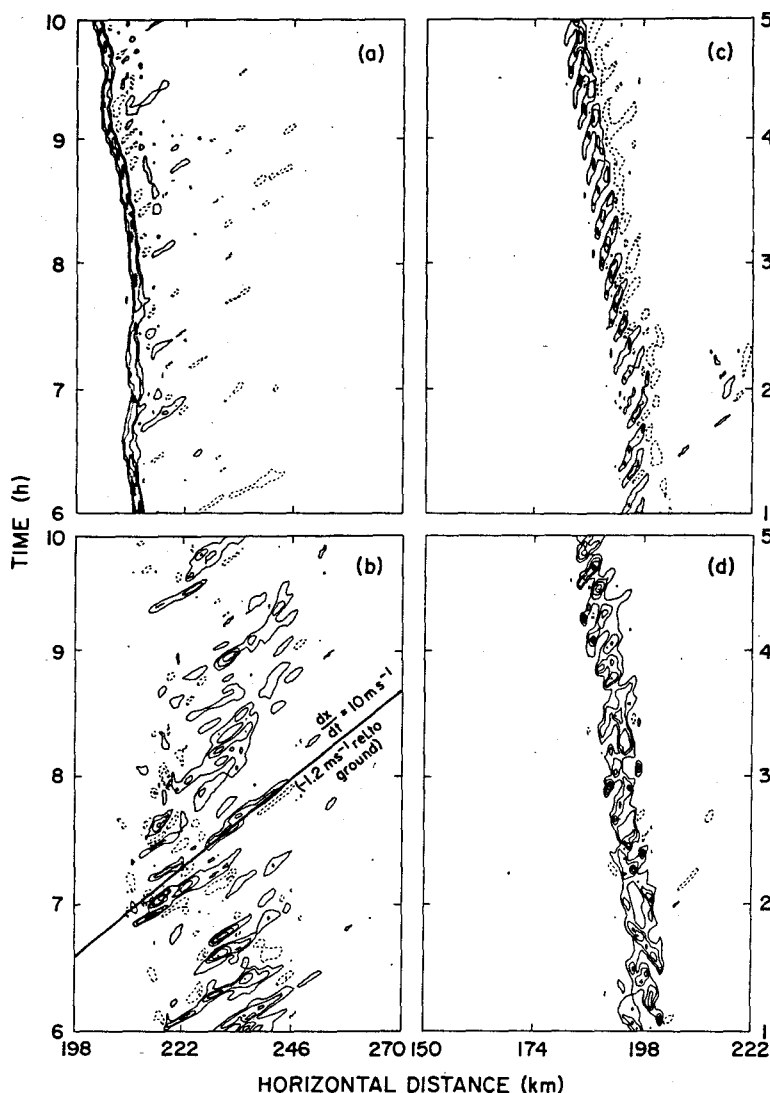


FIG. 14. Time-distance plots of the vertical velocity for part of domain 3: (a) simulation 23U at a height of 1 km, (b) simulation 23U at a height of 6 km, (c) simulation 22ME at a height of 1 km, (d) simulation 22ME at a height of 6 km. The isoline interval is 2 m s^{-1} for (c) and 3 m s^{-1} for (a, b and d) with the first solid line at 1 and 1.5 m s^{-1} , respectively. The Galilean transformations are -11.2 m s^{-1} and -13 m s^{-1} for 23U and 22ME respectively.

described in TMM and RKW. Since the present simulations are consistent with these results, this aspect will only be summarized. Typically, there is a gradual decrease of the vertical velocity, maximum rain mixing ratio, domain-mean vertical velocity and total precipitation rate. As the gust front accelerates, the deep precipitating convective cells increase their travel speed relative to it and the distance between old and new cells increases (Fig. 15a compared to Fig. 1). This is evidenced by the 20 km-long "nose" identifying the envelope of the new developing cells (Fig. 15b) that results in a marked decrease in the mean slope of the ascending air (Fig. 15c). Moreover, the rotor intensifies, widens and merges with the rear-inflow jet which

is markedly lowered (see section 6 and in particular Fig. 21d for further details).

The transition stage is, therefore, structurally distinct from both the growth and mature phases. It could result in: 1) the eventual decay of the system, 2) the assumption of another quasi-steady state, or 3) renewed activity at another location where the environmental conditions are more favorable for deep convection (for instance, increased moisture in the boundary layer). Note that the cold pool is a remarkably persistent dynamical entity that can propagate for great distances as an "outflow boundary" (Wilson and Schreiber 1988) even in the absence of precipitating convection. However, as with the developing stage, detailed observations

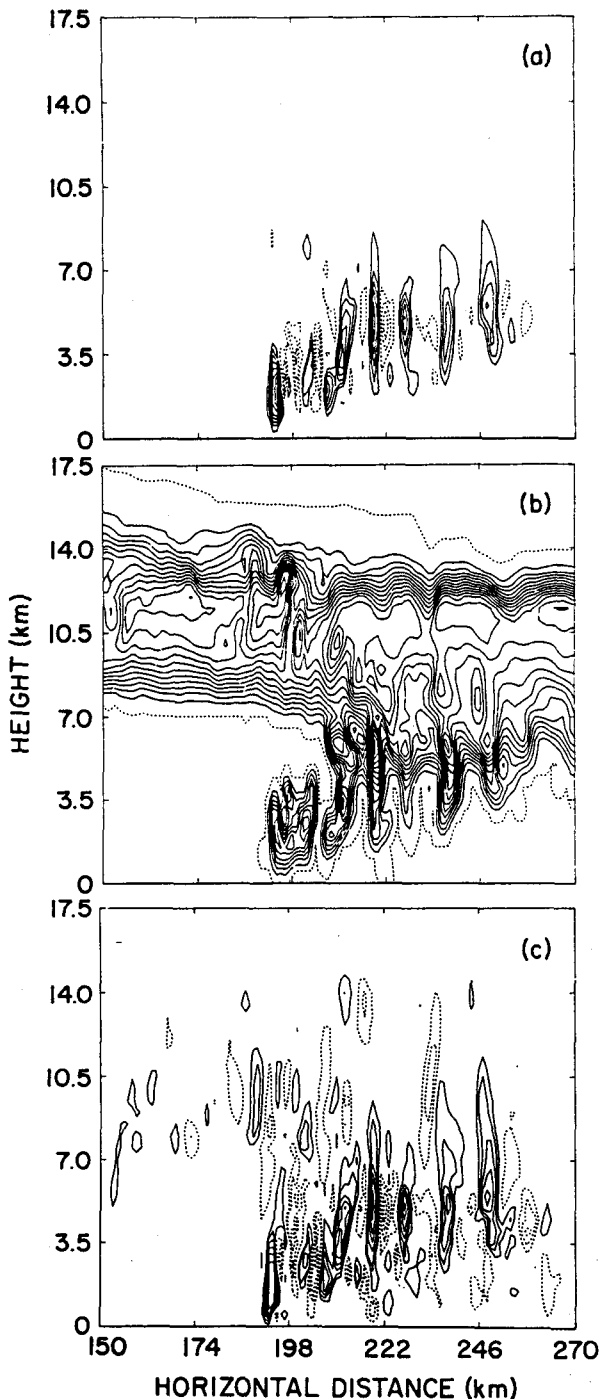


FIG. 15. Transition stage of simulation 23X at 8 h for domain 3: (a) Condensation/evaporation, (b) cloud water, (c) vertical velocity. The isoline intervals are $1.9 \times 10^{-3} \text{ g kg}^{-1} \text{ s}^{-1}$, 0.25 g kg^{-1} and 1 m s^{-1} , respectively. The first solid line at $0.95 \times 10^{-3} \text{ g kg}^{-1} \text{ s}^{-1}$, 0.25 g kg^{-1} and -1 m s^{-1} , respectively. The minimum and maximum vertical velocities are -7.6 and 9.1 m s^{-1} , respectively.

of the transition and decay stages of squall lines are required before meaningful quantitative comparisons of model and observational data can be made.

It is instructive to diagnostically analyze the model fields in terms of Lagrangian concepts because powerful conservation properties can then be employed to determine the overall transport properties of the system. The following two sections will therefore consider Lagrangian passive tracer and vorticity analyses.

5. Tracer analysis of the transports

The Smolarkiewicz (1984) positive definite advection scheme that was generalized in Smolarkiewicz and Clark (1986) was used to calculate the transport of three passive tracers T_i whose conservation equations are

$$\frac{DT_i}{Dt} = 0, \quad i = 1, 2, 3. \quad (3)$$

The tracers are interactively nested and, as shown in Fig. 2a, initialized to unity in three overlying horizontal layers 2 km in depth, but are elsewhere zero. The layers were chosen because they represent the principal zones that feed the convective updrafts and downdrafts and maintain the potential energy supply. These layers also have different shear structure. Tracer 1 is initially distributed in the high θ_e (monsoon flow) layer. The shear is weak up to 1.5 km, approximately the observed depth of the monsoon layer. Tracer 2 is initially contained in the transition layer between the moist monsoon flow and the dry AEJ. It feeds the system from a region of lower θ_e with a strong vertical gradient of θ_e and horizontal windspeed. Tracer 3 initially occupies the driest layer (θ_e minimum and approximately constant). The shear in this layer is of opposite sign to that associated with tracer 2. Since almost all the air entering the system originates from below 6 km, this initial tracer distribution allows the transports to be calculated and to distinguish between rear and front inflows.

The tracer method for quantifying transports is applicable to conservative or quasi-conservative quantities such as mass, equivalent potential temperature, moisture, and passive chemical constituents. However, it should not be used for evaluating momentum transports since these can be due to "action at a distance" such as in wave transports.

a. Tracer concentration

The efficiency of the vertical transport is most clearly demonstrated in simulation 23Z by an analysis of the tracer concentration. In Fig. 16a tracer 1 enters the system and is transported upwards in the updrafts and diluted by upper-level diffluence in the front and rear anvils. The extensive shaded area, enclosed by the 50% concentration isoline, quantifies the effectiveness of the upward transport. The tracer 1 concentration below the rear anvil decreases to low values ($<15\%$).

The concentrations of tracers 2 and 3, initially located in the dry layers between 2–4 km and the 4–6 km layers, respectively, are quite different from tracer

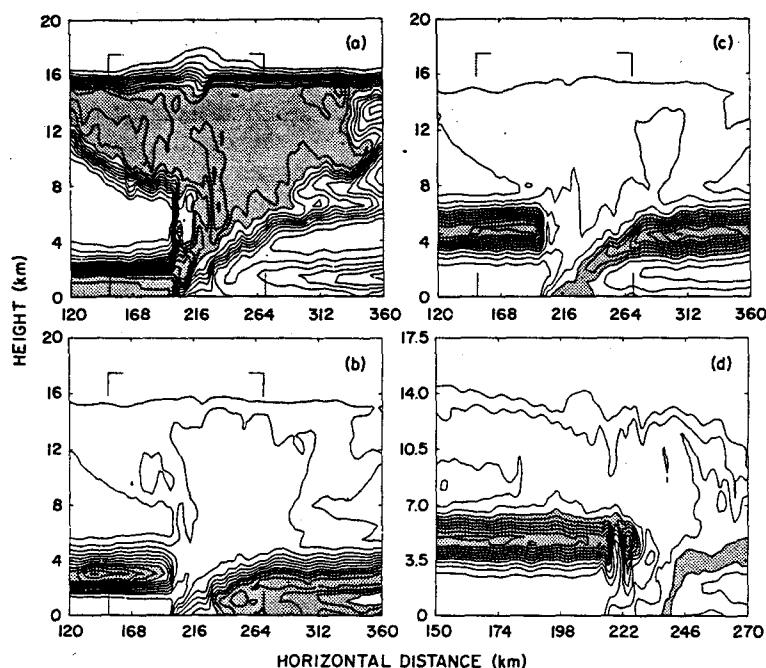


FIG. 16. Tracer fields after 6 h of simulation (a) tracer 1 in simulation 23Z in domain 2, (b) tracer 2 in simulation 23Z in domain 2, and (c) tracer 3 in simulation 23Z in domain 2 and (d) tracer 3 in simulation 23U in domain 3. The dotted regions show where the tracer is in excess of 50% concentration in (a) and (b), 25% in (c) and (d). The isoline interval is 6.25% and the bracketed regions in (a), (b) and (c) correspond to domain 3.

1 (Figs. 16b and 16c). Only a small percentage (about 10% to 15%) reaches the upper levels, whereas a much larger proportion is transported downwards and into the cold pool. Air originating at midlevels therefore influences the mass budget and thermodynamic properties of the cold pool and thereby constitutes a strong feedback to affect convective development. It is difficult to exactly quantify the tracer transport across the stratiform region into the cold pool by the rear-to-front flow, but it is about 25%. However, this is clear evidence of the interaction between the two dominant scales within the system, namely the convective and meso-scale regions. This is a basic and important aspect of the system dynamics and is more apparent in the vorticity analysis of the next section.

The tracer 2 concentration maximum (55%) is attained in the tail part of the density current, while that of tracer 3 is located in the head part and is coincident with the rotor. For 23Z, tracers 2 and 3 enter the system mostly from the rear as shown in Figs. 16b and c. However, this is not universally true because Fig. 16d shows that for simulation 23U, a significant proportion of tracer 3 in domain 3 enters *from ahead of the line* and divides into several pockets. Although not shown here, these subsequently descend and enter the rotor. The distribution of the conserved θ_e field (not shown) is similar to the tracer fields, but the latter yields more quantitative information on the mass transports occurring within the system.

Figure 17 summarizes the density current (defined as the area of negative buoyancy below 2 km) tracer constitution for domain 3 for four different simulations using the 23 June thermodynamics, time-averaged between 6 and 8 h. While the tracer 3 proportion stays approximately constant (20%), the tracer 2 concentration increases monotonically (30% to 47%) as the AEJ initial speed (U_J) increases from -14.1 to -23.8 m s^{-1} . It appears that the downward transport of tracer 2 (but not tracer 3) increases with $-U_J$, consistent with the previous result for the density current formation rate.

The modification of the boundary layer by air originating from just above cloud base is thereby demonstrated, a result that is consistent with the boundary layer transformation by squall lines in the Venezuelan Meteorological and Hydrological Experiment (VIM-HEX) and described by Miller and Betts (1977).

b. Streamfunction analysis of the time-averaged tracer transports

If the system is in a quasi-steady state on a chosen time scale (say 1 h) then the transports during that period will be approximately nondivergent. The fact that this is not exactly satisfied herein (although the errors are only about 10%) can be explained in several ways. First, the computations are not exactly consistent with the model advection scheme. Second, the time

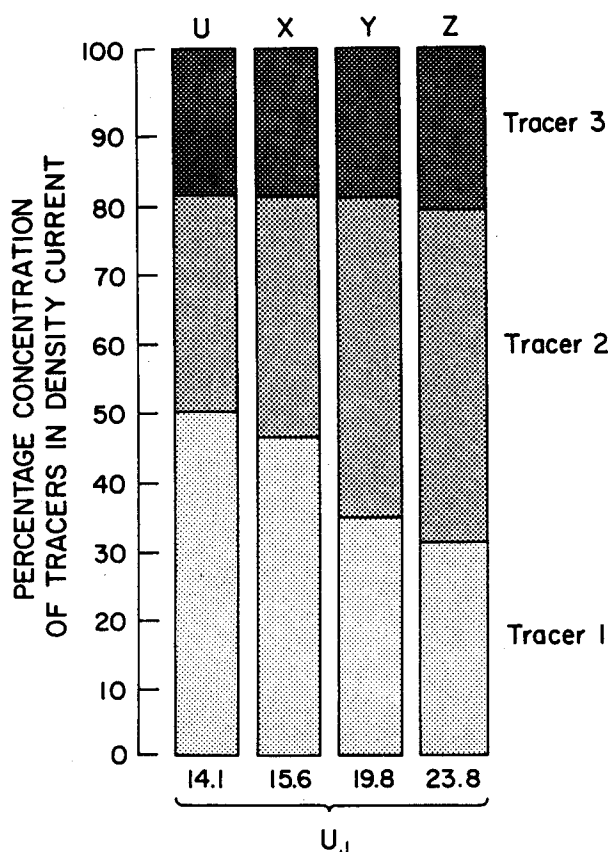


FIG. 17. The percentage tracer concentration within the density current for simulations 23U, 23X, 23Y and 23Z. The values are time- and space-averaged between 6 and 8 h.

resolution of the analysis is 5 min so transient processes on small time scales cannot be represented. Third, the tracer transport is not steady especially at the beginning of the period and, finally, the model Galilean transformation is not exactly equal to the translation speed of the system (-11.2 vs -16.7 m s $^{-1}$ and -11.5 vs -16.2 m s $^{-1}$ for 23U and 23Y, respectively) during the 6–7 h time period in Fig. 18.

A streamfunction for the nondivergent part of the transports was computed and the solution of the resulting elliptic equation is influenced by the boundary conditions. After tests, the tracer mass outflow was chosen to have a zero horizontal gradient while the inflow is fixed at the initial value. Domain 3 tracer fields are presented since this allows a better evaluation of the convective-scale transport.

The tracer transports are summarized in Fig. 18 by showing the streamfunction fields, but this cannot fully represent the physics because transient effects are locally significant in the convective region and result in a localized overturning (as would be evident from a trajectory analysis). The analysis summarizes the two simulations 23U (Figs. 18a, b and c) and 23Y (Figs. 18d, e and f) differing mainly by the intensity of the initial AEJ ($U_j = -14.1$ and -19.8 m s $^{-1}$, respectively).

The total tracer mass gain or loss (residual) at the model 3 domain scale is indicated in the upper left corner of each figure and is at most 18% of the total tracer inflow after 6–7 hours of simulation. It is typically much smaller, showing the significance of the tracer analyses.

The tracer 1 transport shows the same basic behavior in both simulations with general ascent in the mean updraft and horizontal transport in the upper levels in the front and rear anvils. However, the vertical transports are stronger and more efficient for 23Y, while for 23U a smaller proportion of tracer 1 reaches the upper levels and a larger proportion is deposited at low levels behind the convective region. The slope of the transport in the convective region is much less than for simulation 23Y. Moreover, a downward transport coincides with the front anvil immediately ahead of the mean updraft. This is a characteristic of all the simulations and is also evident in the dual-Doppler analysis of Roux (1988). Such subsidence ahead of the squall line was stronger and more widespread for simulations “I” that have smaller precipitation fall speeds. This enhancement is consistent with the evaporation of ice crystals falling from the front anvil.

The numbers within the large arrows in Fig. 18 show the mass fluxes (F_m) across the domain-3 lateral boundaries per unit (1 m) length in the y -direction:

$$F_m(x_b) = \int_{z_1}^{z_2} \rho(z) u_r(x_b, z) dz \quad (4)$$

where u_r is the system-relative horizontal velocity component, x_b the x -coordinate of the domain boundary in question, ρ the air density, and z_1 and z_2 the limits of the vertical column under consideration.

Whereas almost all of tracer 2 enters from ahead of the system in 23U, (9.0 tonne m $^{-1}$ s $^{-1}$ vs 0.7 tonne m $^{-1}$ s $^{-1}$), it originates from both the front and the rear (6.7 tonne m $^{-1}$ s $^{-1}$ vs 5.5 tonne m $^{-1}$ s $^{-1}$) in 23Y. A similar concentration of tracer 2 reaches the upper levels in both cases, but a larger proportion of tracer 2 reaches the density current and is expelled rearward in 23Y. For the 23U simulation, therefore, tracer 2 crosses the convective region from the front, enters the rotor and descends to ground level, whereas the downdraft tracer-2 transport for the 23Y simulation occurs in an overturning downdraft originating from the rear and a downdraft entering from ahead of the system. The latter is, however, not evident in the streamfunction fields because it is an unsteady feature. The tracer-2 and -3 transports are similar and tracer-3 rear inflow is not predominant even in 23Y. For all tracers, a proportion is captured in the density current head region by the rotor circulation and tracer-1 mass transport is at least three times more efficient than the others.

c. Evolution of the total mass inflow

The different structure of the 23U and 23Y simulations is clearly evident in the streamfunction fields in Fig. 18, particularly regarding the origin of the

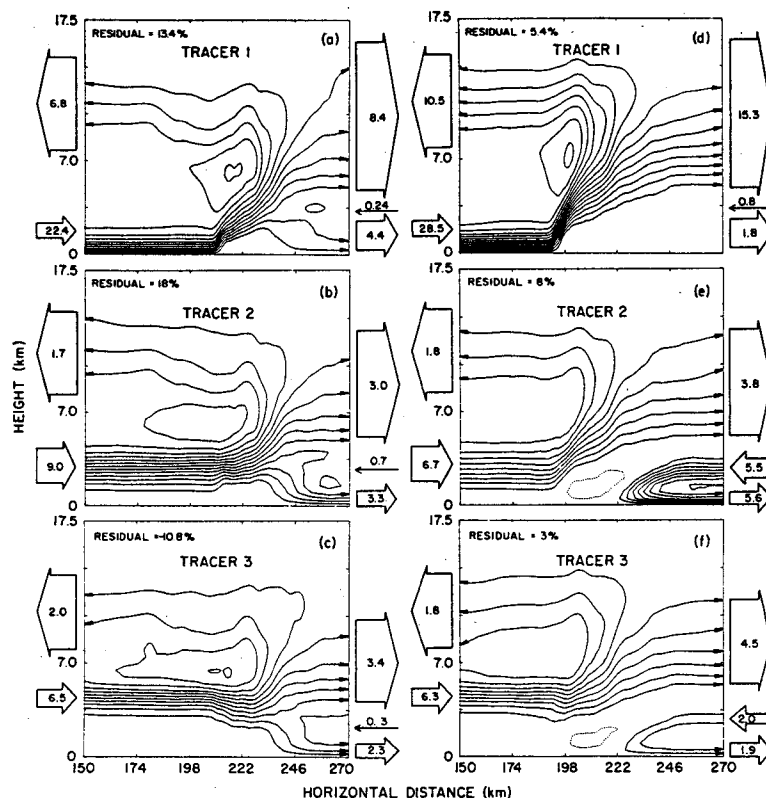


FIG. 18. The streamfunctions for the nondivergent part of the tracer mass transport for the three tracers in the domain-3 (a), (b) and (c) simulation 23U and (d), (e) and (f) simulation 23Y. The isoline interval is three times larger for tracer 1 than for the others. The tracer mass inflow and outflow ($\text{tonne m}^{-1} \text{s}^{-1}$) for physically significant regions at the domain-3 lateral boundaries are represented by the large (block) arrows. The residual of tracer mass is indicated in the upper-left-hand corner of each frame in percent of the total tracer mass inflow. The computations are performed between 6 and 7 h of each simulation with a 5 min time resolution.

downdraft air. This difference is quantified in the evolution of the total mass inflow across the domain-3 lateral boundaries in Fig. 19. The percentages in this figure indicate the rear and/or front inflow between the 2 and 6 km altitudes normalized with respect to the front inflow up to 2 km. Subsequent to the intensification of the density current and the rear inflow merger with the density current head, the system propagation speed increases and the inflow to the downdraft from ahead of the system is enhanced. The 23U simulation has practically no rear inflow but a region of relative flow stagnation develops. Significantly, this simulation enters the transition stage after about 8 h, much earlier than the cases with a strong rear inflow. The mass inflows up to the 6 km level compare favorably to the $58 \text{ tonne m}^{-1} \text{s}^{-1}$ up to the 7 km reported by Chalon et al. (1988).

The system-scale organization can be conceptualized as a superposition of the MM propagating and the Moncrieff and Green [MG] steering-level archetypes schematically shown in Fig. 20. The dominance of either regime depends on the initial wind profile and the age of the system. The 23U case basically represents

propagating behavior (although a weaker steering-level branch does exist), whereas in 23Y the steering-level branch is dominant.

6. Lagrangian vorticity analysis of the flow organization

The buoyancy and vorticity fields of simulation 23Y, averaged during its mature stage between 8 and 10 h, are shown in Figs. 21a and b. The area of positive vorticity centered near 3.5 km is large and well defined. Starting at least 300 km behind the gust front and beneath the rear anvil, the positive vorticity area slopes downwards until at about 50 km behind the gust front it intersects the density current and reaches ground level close to the gust front. A region of intense negative vorticity coincides with the convective downdraft outflow in the density current tail. The strongly sloped transition zone between these two areas corresponds to the axis of the rear-inflow jet. The curl of the updraft outflow in the leading anvil region corresponds to the negative vorticity located above the positive vorticity area.

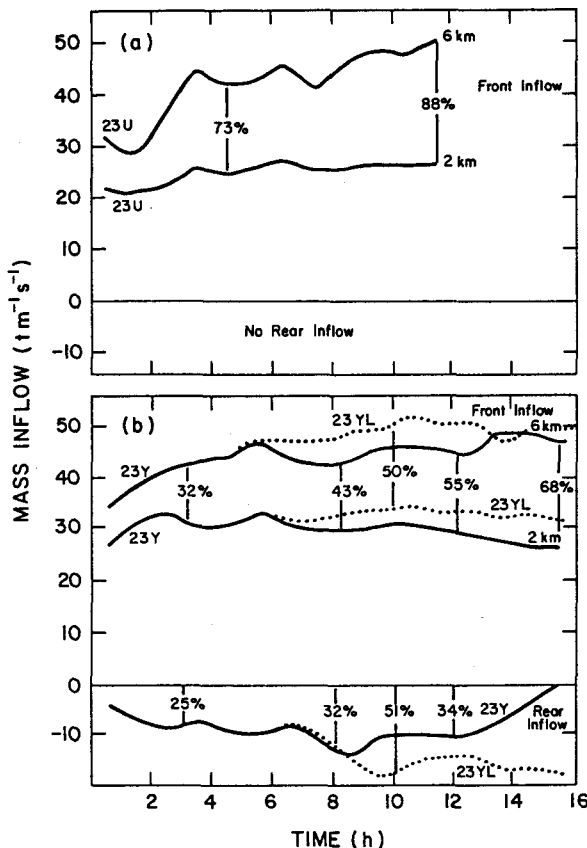


FIG. 19. Evolution of the total tracer mass inflow at the domain-3 lateral boundaries in front of the squall line and up to the 2 km level and the 6 km levels in front of and behind the line, respectively ($\text{tonne m}^{-1} \text{s}^{-1}$). Percentages in the lower part of each frame indicate the proportion of rear inflow and those in the upper part the proportion of the front inflow between 2 and 4 km, as a percentage of the front inflow up to 2 km. Three simulations are shown, (a) 23U, (b) 23Y and (c) 23YL.

The vorticity production by buoyancy gradients (Fig. 21c) is in phase with the vorticity field. Note that the vorticity generation is closely related to the integral of the buoyancy gradients along trajectories, a concept that is mathematically represented below. Since the updraft parcels rapidly traverse an area of strong potential temperature gradient, a marked vorticity generation does not occur. Conversely, the rear inflow remains in a weak potential temperature gradient for a substantial period and thus acquires significant vorticity.

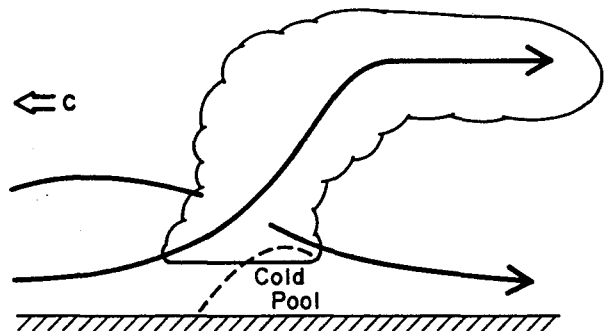
A dynamical interpretation of the system-scale vorticity structure will now be established. In a two-dimensional, steady, inviscid flow there are only two processes that can alter the vorticity of a Lagrangian fluid parcel, namely, the generation of horizontal vorticity by horizontal potential temperature gradients (for brevity this process will be called "baroclinity") and the variation of density with height ("compressibility"). It was shown in an exact nonlinear analysis by MG that by transforming the vorticity equation to stream-

function coordinates, the baroclinic generation can be expressed as a Lagrangian derivative. This leads to the physical concept mentioned above, namely that the vorticity generation can be written as a Lagrangian derivative of the integrated buoyancy gradients along streamlines. The compressibility effect, which is important only if the vertical displacements of parcels are comparable to the density-scale height, can likewise be represented by a Lagrangian derivative as a density weighting of the vorticity (η/ρ). These two processes constitute the physical basis of the MG vorticity conservation theorem for the relative flow,

$$\frac{\eta}{\rho} = \frac{1}{\rho_0} \frac{du_0}{dz_0} - \frac{\text{CAPE}(\psi, z)}{\frac{1}{2} \rho_0 u_0(\psi) \delta(\psi, z)} \quad (5)$$

where $\eta = \partial u / \partial z - \partial w / \partial x$ is the y -component of vorticity, $\delta(\psi, z) = (z - z_0)$ is the displacement of parcels from the (horizontal) inflow height $z_0(\psi)$ of a streamline $\psi = \text{constant}$. In this equation, $u_0(\psi)$ is the relative inflow speed and $\text{CAPE}(\psi, z) = \int_{z_0}^z g \delta \phi dz'$ is the potential energy released as a parcel is vertically displaced by δ along a streamline $\psi = \text{constant}$, where $g \delta \phi$ is the local buoyancy at height z' expressed in terms

(a) Propagating Model



(b) Steering-Level Model

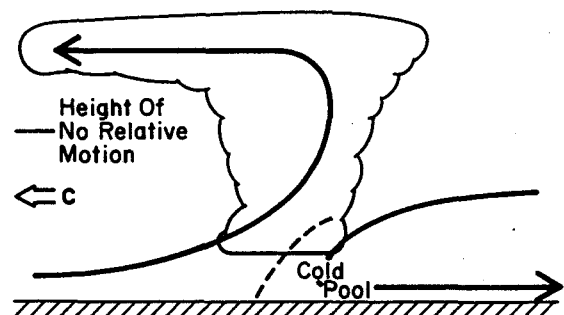


FIG. 20. Schematic diagrams of idealized squall line relative flow (a) propagating model of Moncrieff and Miller (1976) and (b) steering-level model of Moncrieff and Green (1972).

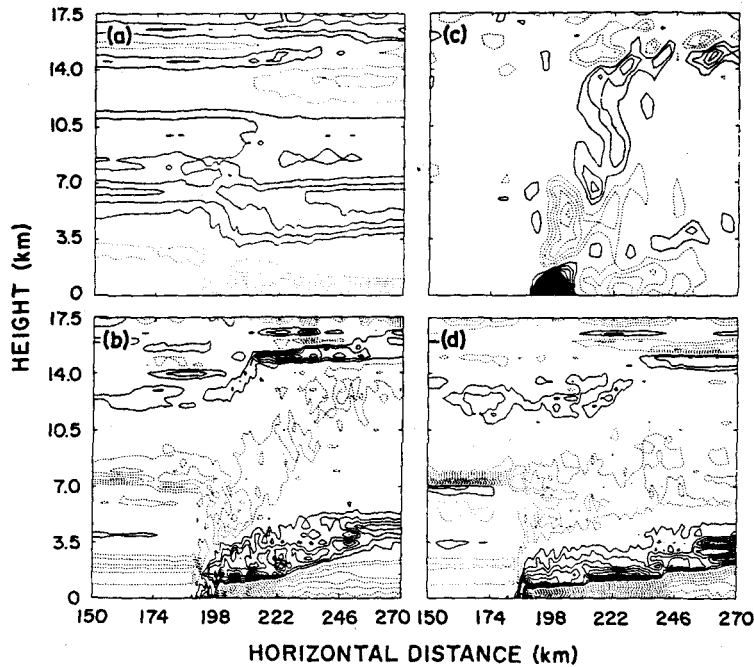


FIG. 21. Time-averaged fields between 8 and 10 h of simulation 23Y at domain-3 scale for (a) buoyancy (K), (b) the along-line horizontal component of vorticity, (c) generation of vorticity by buoyancy gradients, (d) vorticity during the transition stage from 12 to 14 h. The isoline intervals are 1° , $32 \times 10^{-4} \text{ s}^{-1}$, $32 \times 10^{-6} \text{ s}^{-2}$ and $32 \times 10^{-4} \text{ s}^{-1}$, respectively, with the first solid lines are at half the isoline interval. Positive (negative) vorticity is shown by continuous (broken) lines.

of the log-potential temperature perturbation ($\delta\phi$) from the undisturbed reference state. In MG, the parcel lapse rate γ and the static stability B are both constant and $\text{CAPE}(\psi, z) = \frac{1}{2}g(\gamma - B)\delta^2$. The algebraic sum of the density-weighted vorticity and the vorticity generation by the horizontal gradients of potential temperature [represented by the highly nonlinear second term on the right-hand-side of Eq. (5)] is thus conserved along a streamline in a steady flow. If $\text{CAPE}(\psi, z) > 0$ in either ascent or descent then the flow releases potential energy whereas if $\text{CAPE}(\psi, z) < 0$ it is dynamically forced.

First, consider the vorticity associated with downward motion, in which case the displacement $\delta(\psi, z)$ is negative. The positive vorticity in the rotor will be maximized if both terms on the right-hand-side of Eq. (5) are positive. The inflow shear in the AEJ is positive in the 3.5–5.5 km layer, but the baroclinic generation is more difficult to determine uniquely. Three distinct origins for the positive vorticity for the rotor can be identified as shown in Fig. 22. First, if the downdraft inflow enters from ahead of the system (u_0), positive vorticity will be generated if the downdrafts are convectively driven [$\text{CAPE}(\psi, z) > 0$]. Second, if parcels originate from the rear (u_0 negative), positive vorticity will be produced if the descent is dynamically forced, [$\text{CAPE}(\psi, z) < 0$]. Third, a local source of positive vorticity in the rotor is demonstrated by considering a typical streamline $\psi_1 = \text{constant}$ in the descending

branch of the rotor in Fig. 22. For this streamline, u_0 is positive and if the descending motion is convectively driven by evaporation and precipitation drag then $\text{CAPE}(\psi, z) > 0$ and positive vorticity will thus be generated.

The positive vorticity generation in the region of dynamically forced subsidence coinciding with the mesoscale rear inflow indicated by the tracer analysis in Fig. 16b and c is very evident in Fig. 21b. This positive vorticity can be explained as a baroclinic generation in an analogous fashion to that described above.

The negative vorticity in the lower levels behind the rotor is due to a baroclinic generation in the convective-scale downdrafts, quantified by again referring to Eq. (5). For a typical streamline in Fig. 22 associated with the overturning downdraft (say $\psi_2 = \text{constant}$), $u_0 < 0$ and $\text{CAPE}(\psi, z) > 0$ and it follows that the vorticity generation will be negative.

Second, consider the convective-scale updraft displacements in which $\delta(\psi, z)$ and $\text{CAPE}(\psi, z)$ are both positive. Since the inflow to both steering-level and propagating overturning updraft branches (as defined in Fig. 19) is from ahead of the system, u_0 is positive. It follows from Eq. (5) that because the inflow vorticity and the vorticity production are both negative in the individual updraft branches, the outflow vorticity must therefore be negative.

These general dynamical principles, based on a diagnostic interpretation of a steady-state Lagrangian

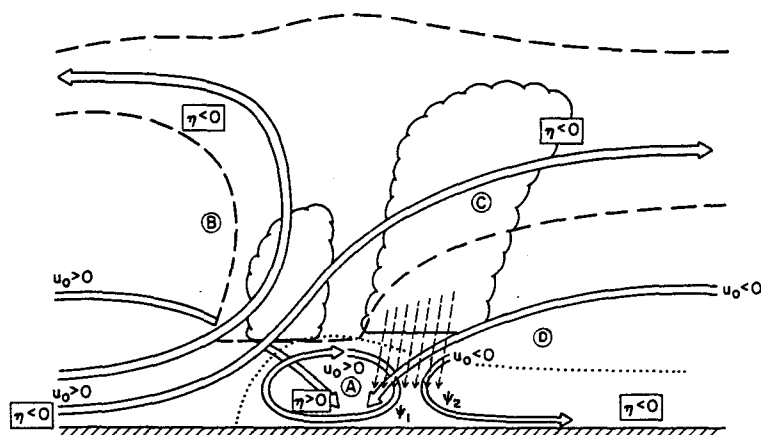


FIG. 22. Schema of the relative flow and vorticity in a squall line system consisting of an unsteady convective region and a quasi-steady mesoscale region. Region A: the rotor with predominately positive vorticity and positive vorticity generation; region B: the overturning updraft; region C: the propagating updraft; region D: the mesoscale descent. The unsteady inflow to the downdraft, the rotor, and the rearward-moving convective-scale downdraft outflow are maintained by evaporative cooling and water-clooding. The outlines of convective cells are shown by scalloped lines, the envelope of the cell aggregate representing the mesoscale system by the broken lines and the outline of the density current by the dotted lines, respectively.

vorticity theorem are remarkably consistent with the model results shown in Fig. 21 despite the local unsteadiness of the convective region. Nevertheless, such *local unsteadiness is essential for existence of the cross-over (RL) of the downdraft inflow from ahead of the system into the precipitation area that results in evaporative cooling in the descending branch of the rotor.* This subtle cooperation between local unsteadiness and system-scale persistence is being quantified in a separate analytical investigation.

The upper-level positive vorticity generation in Fig. 21c is another distinctive feature and may be due to the horizontal gradient of buoyancy between the overturning and propagating updrafts arising from the overturning updraft being potentially warmer than the propagating one at a given height. This can be represented in a near-field steady analytic model by extending on the approach used in Moncrieff (1978).

a. Role of system-scale vorticity

As was concluded in TMM and RKW, strong low-level shear and its interaction with the cold pool is important for maintaining cell development and it would be disingenuous to dismiss its role on the convective-scale organization. However, the generation of new cells is only part of the problem of sustaining a persistent mesoscale convective system. The above analysis shows that a complete description of the vorticity field in squall-line-type convective systems and its relationship to longevity is more complex than a local balance between the low-level inflow shear and the vorticity generation associated with the cold pool as hypothesized by RKW. *An important result is that it is an oversimplification to say that the interaction of*

the shear and the cold pool adequately explains the longevity of a mesoscale convective system because the organization of the vorticity field is predominantly on the scale of the entire system and not confined to a localized convective scale. This is clearly demonstrated by the above Lagrangian analysis that shows the subtle interaction between the convective and mesoscale regions of the squall system.

b. Vorticity structure during the transition stage

Figure 21d illustrates the change in the vorticity field as the system undergoes a transition to a more horizontally orientated entity. The rearward mid- to upper-level negative vorticity area is lowered, consistent with the decrease in the mean updraft slope. The altitude of the positive vorticity layer below the rear anvil is also lower (about 1.5 km) corresponding to the decreased elevation of the rear inflow. The rotor is extensive and results in the density current leading edge being accelerated forward, consistent with the remarks in section 4b. Lafore et al. (1988) noticed a similar evolution over a 1 h period in a Doppler radar analysis that was characterized by a decrease of the convective cell zone slope, the intensification of the rotor in lower levels and the front-to-rear circulation in upper levels.

7. Conclusions

The squall line convective system causes a large-magnitude upscale influence on the environment for several hundred kilometers, particularly to its rear, and the momentum perturbations are of comparable magnitude to the local mean flow. This upscale influence has important implications regarding the parameterization of momentum and vorticity transports because

it cannot be considered as a subgrid scale process in large-scale models. An alternative method for representing the dynamical transports by mesoscale convective systems is therefore essential.

Horizontal potential temperature gradients generated by a combination of latent heat release in the convective region and unsaturated mesoscale descent, both modulated by evaporation, cause a horizontal pressure gradient and the mesoscale rear inflow is a consequence of these processes. Ahead of the system the AEJ strength is reduced and the TEJ is enhanced, while in the rear the TEJ is reduced and the AEJ is enhanced. The velocity perturbation below 4 km, due to the rear inflow, is the most marked signature in the horizontal momentum change.

The mesoscale and the convective-scale organization have both been quantified and there is a strong interaction between these two dominant scales. The use of a large domain allows an explicit representation of the mesoscale features and the modifications of the AEJ and TEJ are in general agreement with observations. The modifications are, however, weakly time dependent and increase with the maturity of the system. The intensity of the rear-to-front wind perturbation behind the system increases with the initial convective instability (CAPE) and is a linear function of the initial AEJ speed. The pressure gradient force accelerates the mesoscale rear inflow at a rate of about $1 \text{ m s}^{-1} \text{ h}^{-1}$. However, the rear-inflow jet can also be interpreted in terms of a vorticity theorem [Eq. (5)]. In either case, the important physics are due to the horizontal gradients of total buoyancy caused by a combination of convective latent heat release, evaporation, mesoscale ascent, and subsidence.

It was also shown by using a simple empirical parameterization of ice-phase physics, namely a reduction of the precipitation fall speed, that microphysical processes can modulate the intensity of this mesoscale wind perturbation through its influence on total buoyancy. This will be helpful in interpreting more complete ice-physics parameterizations. Diabatic processes such as the differential radiation (McBride and Gray 1980) between the anvil and the surrounding clear air are likely to enhance the buoyancy contrast. With the warm rain parameterization employed here, the mesoscale vertical velocities are too weak and localized when compared to observations; inclusion of more realistic ice physics should improve this comparison.

If precipitation evaporation below the anvil is enhanced then the mesoscale subsidence becomes more widespread and intense and the system is somewhat less well organized. This is a paradox because the general opinion is that a system will be better organized and more intense if its mesoscale rear subsidence is stronger. Increased evaporation decreases the mesoscale pressure gradient and the rear inflow that can promote convective development through its enhancement of the low-level convergence by a blocking effect arising from the enhancement and subsidence of the AEJ. Furthermore,

if stronger subsidence exists, then the rear-to-front circulation will be lowered (see Fig. 11b) and be less efficient in releasing the convective instability.

The convective-scale organization is predominately in the form of transient cells that travel backwards relative to the gust front at a speed of about 10 m s^{-1} . The exception to this behavior is when the inflow shear above the AEJ is sufficiently decreased in which case the density current is replaced by a transient, wavelike low-level convergence conceptually similar to the solitary wave reported in DMS, which is a special case.

In certain simulations, particularly when the AEJ is strong, the convective-scale downdrafts originate from ahead of the line and periodically form pockets of cold air that are out of phase with the cell development. Observations show that such multicellular behavior is a real feature of squall line behavior (Zipser 1969, 1977). Downdraft inflow can enter the cold pool from ahead of a propagating system if the flow is either three-dimensional or two-dimensional and unsteady. The system is clearly unsteady on the convective scale but the mesoscale vorticity field is remarkably persistent or quasi-steady. The morphology of the constructive interaction between these regions is conceptually represented in Fig. 22. *The organized nature of the system-scale vorticity quantifies the complex dynamical interaction between the convective and mesoscale (stratiform) regions.* The presence of which has been implied by observations for many years, for example by Houze, Zipser and colleagues.

Localized forcing at the cold pool and its role in the triggering of convection cells was shown by TMM and RKW (both papers concentrated on the convective part of the system) to be important to the longevity of the subset of squall lines that do not contain extensive stratiform regions. Although substantial low-level shear features in the COPT81 cases, *it is repudiated as a sufficient condition for their longevity because of the interaction between the convective and stratiform regions, for instance as evidenced by the system-scale vorticity generation.* This emphasizes the "global" as opposed to the "local" physics of the system. Moreover, the convergence effected by the rear inflow is another mechanism for forcing and maintaining the convective-scale activity, separate in both scale and dynamics from the cold pool forcing.

It is concluded that in convective systems containing pronounced mesoscale circulations, the local triggering at the gust front only partly explains the persistence of convective activity for a period far exceeding individual cell lifetimes. This has been demonstrated herein by numerical experimentation. Analytical models are now being developed to understand the basic physics of the organization of mesoscale convective systems consisting of populations of cells and a marked stratiform region.

Acknowledgments. We thank Terry Clark, Bill Hall and Piotr Smolarkiewicz for their invaluable assistance

and advice with modeling problems. We also thank Terry Clark, Brant Foote, and Peggy LeMone for their comments. One of the anonymous reviewers is acknowledged for his particularly constructive criticisms that considerably improved the text. Andy Heymsfield advised us on the empirical formulation of the ice physics parameterization. The work was undertaken during J.-P.L.'s long-term visit to the Cloud Systems Division, NCAR and was partly supported by the Centre National de Recherche Météorologiques (DMN/EERM) and the Institut National des Sciences de l'Univers, Paris (ATP RA No. 5610).

REFERENCES

- Betts, A. K., R. W. Grover and M. W. Moncrieff, 1976: Structure and motion of tropical squall lines over Venezuela. *Quart. J. Roy. Meteor. Soc.*, **102**, 395–404.
- Chalon, J.-P., F. Roux, G. Jaubert and J.-P. Lafore, 1988: The West African squall line observed on 23 June during COPT81. *J. Atmos. Sci.*, **45**, 2744–2763.
- Chen, S., and W. R. Cotton, 1986: Preprints, *Joint Conferences on Radar Meteorology and Cloud Physics*, Snowmass, 3, 1183–1186.
- Cho, H.-R., and T. L. Clark, 1981: A numerical investigation of the structure of vorticity fields associated with a deep convective cloud. *Mon. Wea. Rev.*, **109**, 1654–1670.
- Chong, M., P. Amayenc, G. Scialom and J. Testud, 1987: A tropical squall line observed during the COPT81 experiment in West Africa. Part I: Kinematic structure inferred from dual-Doppler radar data. *Mon. Wea. Rev.*, **115**, 670–694.
- Clark, T. L., 1977: A small-scale dynamic model using a terrain-following coordinate transformation. *J. Comput. Phys.*, **24**, 186–215.
- , 1979: Numerical simulations with a three-dimensional cloud model: lateral boundary condition experiments and multicellular severe storm simulations. *J. Atmos. Sci.*, **36**, 2191–2215.
- , and R. D. Farley, 1984: Severe downslope windstorm calculations in two and three spatial dimensions using anelastic interactive grid nesting: a possible mechanism for gustiness. *J. Atmos. Sci.*, **41**, 329–350.
- Crook, N. A., and M. J. Miller, 1985: A numerical and analytical study of atmospheric undular bores. *Quart. J. Roy. Meteor. Soc.*, **104**, 225–242.
- Dudhia, J., M. W. Moncrieff and D. W. K. So, 1987: The two-dimensional dynamics of West African squall lines. *Quart. J. Roy. Meteor. Soc.*, **113**, 121–146.
- Gamache, J. F., and R. A. Houze, 1982: Mesoscale air motions associated with a tropical squall line. *Mon. Wea. Rev.*, **110**, 118–135.
- Houze, R. A., 1977: Structure and dynamics of a tropical squall line system. *Mon. Wea. Rev.*, **105**, 1540–1567.
- von Karman, T., 1940: The engineer grapples with non-linear problems. *Bull. Amer. Math. Soc.*, **46**, 615–626.
- Lafore, J. P., J. L. Redelsperger and G. Jaubert, 1988: Comparison between a three-dimensional simulation and Doppler radar data of a tropical squall line: transports of mass, momentum, heat and moisture. *J. Atmos. Sci.*, **45**, 3483–3500.
- LeMone, M. E., G. M. Barnes, and E. J. Zipser, 1984: Momentum fluxes by lines of cumulonimbus over the tropical oceans. *J. Atmos. Sci.*, **41**, 1914–1932.
- McBride, J. L., and W. M. Gray, 1980: Mass divergence in tropical weather systems. Paper 1: Diurnal variation. *Quart. J. Roy. Meteor. Soc.*, **106**, 501–516.
- Miller, M. J., and R. P. Pearce, 1974: A three-dimensional primitive equation model of cumulonimbus convection. *Quart. J. Roy. Meteor. Soc.*, **100**, 133–154.
- , and A. K. Betts, 1977: Traveling convective storms over Venezuela. *Mon. Wea. Rev.*, **105**, 833–848.
- Moncrieff, M. W., 1978: The dynamical structure of two-dimensional steady convection in constant vertical shear. *Quart. J. Roy. Meteor. Soc.*, **104**, 543–567.
- , 1981: A theory of organised steady convection and its transport properties. *Quart. J. Roy. Meteor. Soc.*, **107**, 29–50.
- , 1985: Steady convection in pressure coordinates. *Quart. J. Roy. Meteor. Soc.*, **111**, 857–866.
- , and J. S. A. Green, 1972: The propagation and transfer properties of steady convective overturning in shear. *Quart. J. Roy. Meteor. Soc.*, **98**, 336–352.
- , and M. J. Miller, 1976: The dynamics and simulations of tropical cumulonimbus and squall lines. *Quart. J. Roy. Meteor. Soc.*, **104**, 543–567.
- , and D. W. K. So, 1989: A hydrodynamical theory of conservative bounded density currents. *J. Fluid. Mech.*, **198**, 177–197.
- Newton, C. W., 1950: Structure and mechanisms of the prefrontal squall line. *J. Meteor.*, **7**, 210–222.
- , 1963: Dynamics of severe convective storms. *Meteor. Monogr.*, **5**, 33–58.
- Nicholls, M. E., 1988: A comparison of the results of a two-dimensional numerical simulation of a tropical squall line with observations. *Mon. Wea. Rev.*, **116**, 3055–3077.
- Ogura, Y., and M.-T. Liou, 1980: The structure of a mid-latitude squall line: A case study. *J. Atmos. Sci.*, **37**, 553–567.
- Redelsperger, J. L., and J. P. Lafore, 1988: A three-dimensional simulation of a tropical squall line: convective organization and thermodynamic vertical transport. *J. Atmos. Sci.*, **45**, 1334–1356.
- Rotunno, R., J. B. Klemp and M. E. Weisman, 1988: A theory of strong long-lived squall lines. *J. Atmos. Sci.*, **45**, 463–485.
- Roux, F., 1988: The West African squall line observed on 23 June during COPT81: Kinematic and thermodynamics of the convective region. *J. Atmos. Sci.*, **45**, 406–426.
- , J. Testud, M. Payen and B. Pinty, 1984: West African squall-line thermodynamic structure retrieved from dual-Doppler radar observations. *J. Atmos. Sci.*, **41**, 3104–3121.
- Rutledge, S. A., 1986: A diagnostic modeling study of the stratiform region associated with a tropical squall line. *J. Atmos. Sci.*, **43**, 1337–1358.
- Soong, S. T., and W. K. Tao, 1984: A numerical study of the vertical transport of momentum in a tropical rainband. *J. Atmos. Sci.*, **41**, 1049–1061.
- Smolarkiewicz, P. K., 1984: A fully multidimensional positive definite advection transport algorithm with small implicit diffusion. *J. Comput. Phys.*, **54**, 325–362.
- , and T. L. Clark, 1986: The multidimensional positive definite advection transport algorithm: Further development and applications. *J. Comput. Phys.*, **67**, 396–438.
- Smull, B. F., and R. A. Houze, 1985: A midlatitude squall line with a trailing region of stratiform rain: Radar and satellite observations. *Mon. Wea. Rev.*, **113**, 117–133.
- , 1987a: Dual-Doppler radar analysis of a midlatitude squall line with a trailing region of stratiform rain. *J. Atmos. Sci.*, **43**, 356–377.
- , 1987b: Rear inflow in squall lines with trailing stratiform precipitation. *Mon. Wea. Rev.*, **115**, 2869–2889.
- Thorpe, A. M., M. J. Miller and M. W. Moncrieff, 1982: Two-dimensional convection in nonconstant shear: A model of midlatitude squall lines. *Quart. J. Roy. Meteor. Soc.*, **108**, 739–762.
- Yoshizaki, M., 1986: Numerical simulations of tropical squall-line clusters: Two-dimensional model. *J. Meteor. Soc. Japan*, **64**, 469–491.
- Wilson, J. W., and W. E. Schreiber, 1986: Initiation of convective storms at radar-observed boundary-layer convergence lines. *Mon. Wea. Rev.*, **114**, 898–915.
- Zipser, E. J., 1969: The role of organized unsaturated convective downdrafts in the structure and rapid decay of an equatorial disturbance. *J. Appl. Meteor.*, **8**, 799–814.
- , 1977: Mesoscale and convective-scale downdrafts as distinct components of squall-line structure. *Mon. Wea. Rev.*, **105**, 1568–1589.
- , R. J. Meitin and M. A. Lemone, 1981: Mesoscale motion fields associated with a slowly-moving GATE convective band. *J. Atmos. Sci.*, **38**, 1725–1750.